iScience

CellPress

Article

Three-Dimensional Hierarchical Porous Nanotubes Derived from Metal-Organic Frameworks for Highly Efficient Overall Water Splitting

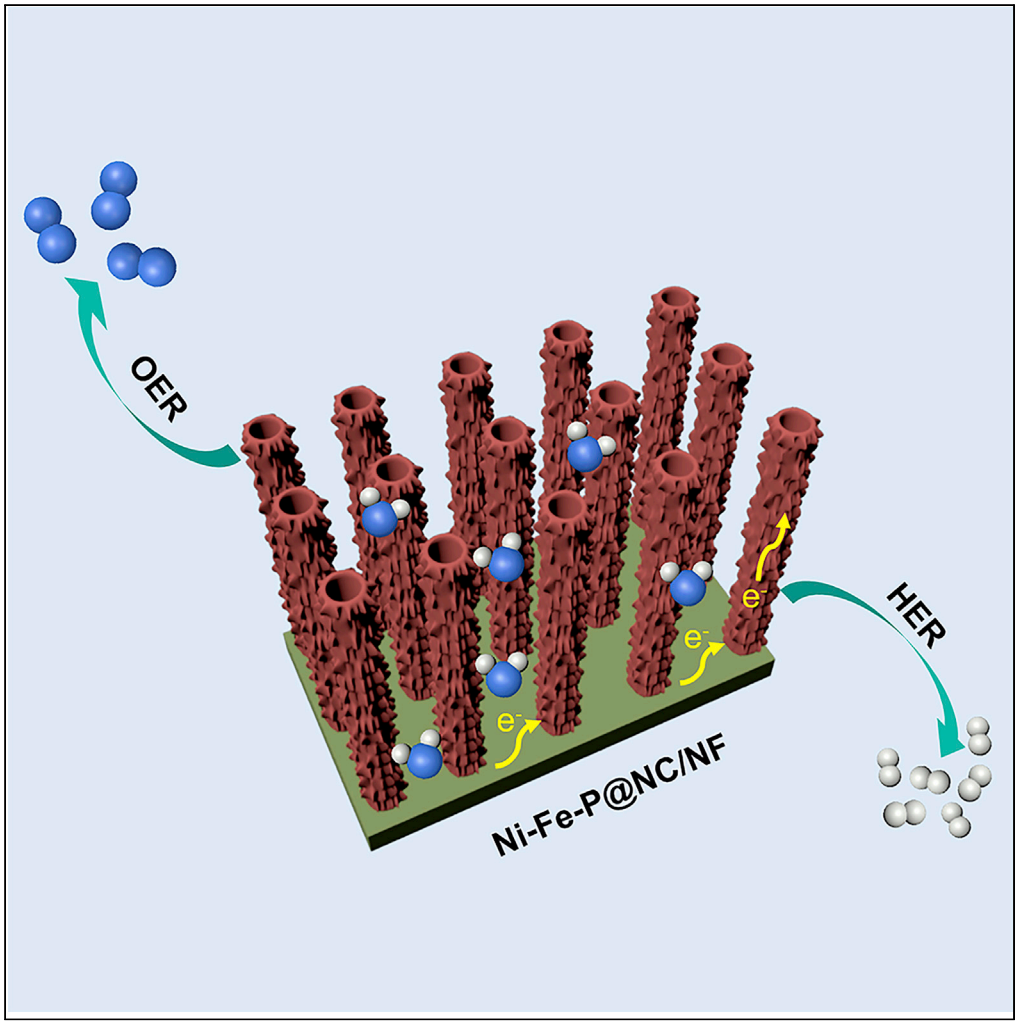

Yang Wang, Shenlong Zhao, Yinlong Zhu, ..., Jing Tang, Dongyuan Zhao, Cordelia Selomulya

jingtang@stanford.edu (J.T.)
dyzhao@fudan.edu.cn (D.Z.)
cordelia.selomulya@monash.edu (C.S.)

HIGHLIGHTS

Nanotubular Prussian blue analogue as a precursor is synthesized by anion exchange

The catalyst exhibits excellent catalytic activity for hydrogen and oxygen production

The catalyst-based electrolyser has a low cell voltage of 1.47 V to obtain 10 mA cm^{-2}

The electrolyser shows an extremely excellent durability for 100 h at 50 mA cm^{-2}

Wang et al., iScience *23*, 100761
January 24, 2020
https://doi.org/10.1016/j.isci.2019.100761

iScience

CellPress

Article

Three-Dimensional Hierarchical Porous Nanotubes Derived from Metal-Organic Frameworks for Highly Efficient Overall Water Splitting

Yang Wang,[1,7] Shenlong Zhao,[3,7] Yinlong Zhu,[1,7] Ruosang Qiu,[1] Thomas Gengenbach,[4] Yue Liu,[1] Lianhai Zu,[1] Haiyan Mao,[5] Huanting Wang,[1] Jing Tang,[2,8,*] Dongyuan Zhao,[1,6,*] and Cordelia Selomulya[1,*]

SUMMARY

Effective design of bifunctional catalysts for both hydrogen evolution reaction (HER) and oxygen evolution reaction (OER) is important but remains challenging. Herein, we report a three-dimensional (3D) hierarchical structure composed of homogeneously distributed Ni-Fe-P nanoparticles embedded in N-doped carbons on nickel foams (denoted as Ni-Fe-P@NC/NF) as an excellent bifunctional catalyst. This catalyst was fabricated by an anion exchange method and a low-temperature phosphidation of nanotubular Prussian blue analogue (PBA). The Ni-Fe-P@NC/NF displayed exceptional catalytic activity toward both HER and OER and delivered an ultralow cell voltage of 1.47 V to obtain 10 mA cm^{-2} with extremely excellent durability for 100 h when assembled as a practical electrolyser. The extraordinary performance of Ni-Fe-P@NC/NF is attributed to the abundance of unsaturated active sites, the well-defined hierarchical porous structure, and the synergistic effect between multiple components. Our work will inspire more rational designs of highly active non-noble electrocatalysts for industrial energy applications.

INTRODUCTION

Direct production of hydrogen from water *via* electricity (i.e. electrolyser cells) is a promising alternative to the route that hydrogen is generated from the traditional steam-reforming of fossil fuels, due to its low cost, high efficiency, and zero-carbon emission. Currently, noble metals (i.e. Pt- and Ru-based catalysts) are the most widely used catalysts in hydrogen and oxygen evolution processes. However, these metal-based catalysts often suffer from multiple disadvantages, including their high cost, poor durability, and low selectivity, which impede commercialization of renewable energy technologies (Long et al., 2019b; Yin et al., 2015; Zhu et al., 2019b). In contrast, earth-abundant materials (transition metal oxides (Zhu et al., 2019a), chalcogenides (Panda et al., 2017; Yin et al., 2017), borides (Masa et al., 2016), phosphides (Zhang et al., 2016a), nitrides (Zhang et al., 2016b), carbides (Wu et al., 2015), etc.) are regarded as the alternatives to replace the noble catalysts. However, due to the lack of rational design in electronic and geometric structure, the activity and durability of these existing non-noble metal-based electrolysers still cannot satisfy the demand for the practical applications. Therefore, it is highly desirable to develop a novel design strategy to construct effective bifunctional electrocatalysts with both HER and OER performance for overall water splitting.

Hollow structure with high exposed surface area is desirable for the design of electrocatalysts where catalytic reactions tend to take place at the surface of the catalysts. However, most nano-tubular materials have been prepared through a template-directed method where the removal of template renders the synthesis process more complex. What is worse, the incorporation of other favorable elements into the tubular materials could make the overall fabrication procedure more complicated. Fortunately, this problem could be solved by utilizing nano-tubular metal-organic frameworks that were synthesized for the first time, as the precursors for the design of target catalysts.

The emerging metal-organic frameworks (MOFs), consisting of organic ligands and metal atom nodes, have displayed the incomparable advantages for various catalytic reactions due to their well-defined structure, controllable elements, and high surface area (Anandhababu et al., 2018; Cai et al., 2017; Fang et al., 2017; Han et al., 2016; Hou et al., 2015; Jiao et al., 2016; Long et al., 2019a; Zhao et al., 2014, 2016; Zheng et al., 2019). Distinct to the widely reported MOFs such as zeolitic imidazolate frameworks (ZIFs)

[1]Department of Chemical Engineering, Monash University, Clayton, VIC 3800, Australia

[2]Department of Materials Science and Engineering, Stanford University, Stanford, CA 94305, USA

[3]The University of Sydney, School of Chemical and Biomolecular Engineering, Sydney, NSW 2006, Australia

[4]Manufacturing, Commonwealth Scientific and Industrial Research Organisation, Clayton, VIC 3168, Australia

[5]Department of Chemical and Biomolecular Engineering, University of California, Berkeley, Berkeley, CA 94720, USA

[6]Department of Chemistry, Laboratory of Advanced Materials, iChEM (Collaborative Innovation Center of Chemistry for Energy Materials), Fudan University, Shanghai 200433, P.R. China

[7]These authors contributed equally

[8]Lead Contact

*Correspondence: jingtang@stanford.edu (J.T.), dyzhao@fudan.edu.cn (D.Z.), cordelia.selomulya@monash.edu (C.S.)

https://doi.org/10.1016/j.isci.2019.100761

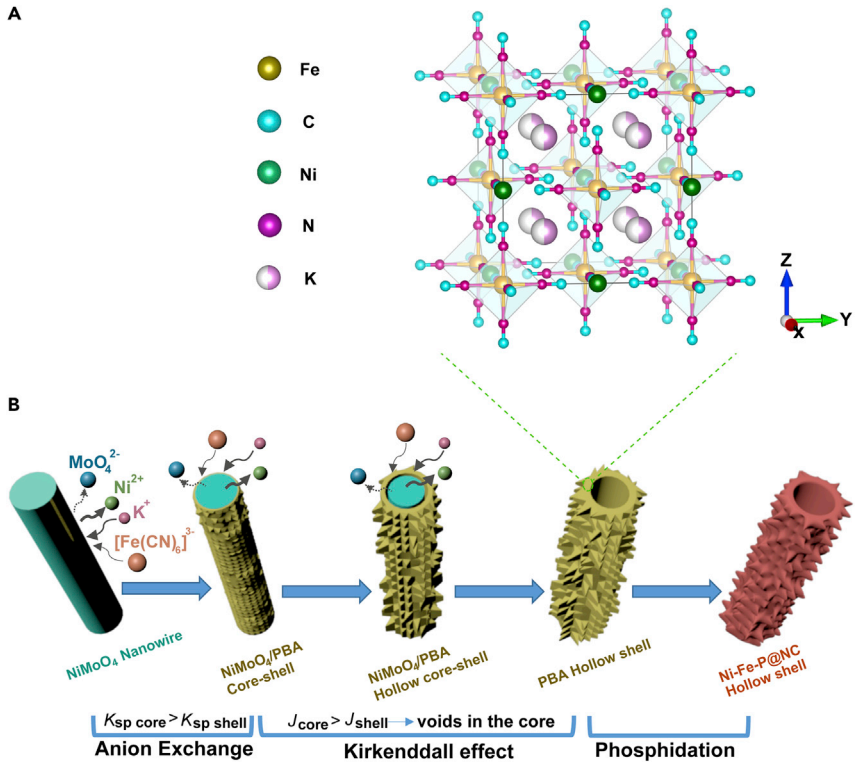

Figure 1. Crystal Structure and Synthesis Process

(A) Crystal structure of $KNi[Fe(CN)_6]$ (PBA).

(B) Schematic illustration of the synthesis process of Ni-Fe-P@NC nanotubes (K_{sp}: solubility product; J: ion transfer rate).

(Anandhababu et al., 2018; Hou et al., 2015) with single metal species, Prussian blue analogues (PBAs) with a generic formula $A_xM_y[Fe(CN)_6]_z \cdot nH_2O$ (x, y, and z are stoichiometric numbers; A is alkali metal cation, and M is a transition metal) (de Tacconi et al., 2003) could be an effective precursor to acquire MOFs-based high-performance electrocatalysts because they possess the following merits: the controllable metal species in PBAs provide an ideal platform to engineer the geometric structure of the active sites at the atomic level, thereby forming the specific nanostructures and morphologies (Ahn et al., 2018; Nai et al., 2018); distinct surface atomic structures and bonding arrangements allow us to obtain high-performance heteroatom-doped electrocatalysts if the porosity and uniformity of the catalytic active sites can be inherited after pyrolysis (Ge et al., 2018); the micro-/meso-pores and high surface area could facilitate the active site's exposure, mass transfer of electrolytes, as well as diffusion of the generated gas (e.g. oxygen and hydrogen) during overall water splitting process (Yu et al., 2016b).

Herein, for the first time, the hollow structural heteroatom-doped carbon nanotubes (Ni-Fe-P@NC) were synthesized by one-step phosphidation of the PBA precursor for efficient overall water splitting. The synthesis process of the Ni-Fe-P@NC is well illustrated in Figure 1. Thanks to the adjustability of the metal sites, the $NiMoO_4$ nanowires were used as a template to fabricate the hollow $KNi[Fe(CN)_6]$ nanotubes *via* an anion exchange method with Kirkendall effect and Ni-Fe-P@NC could then be obtained by a low-temperature phosphidation. The resultant Ni-Fe-P@NC nanotubes with a nano-porous wall consisting of Ni-Fe-P nanoparticles in nano-carbons on nickel foam are demonstrated to be robust electrocatalysts for both HER and OER. Ni-Fe-P@NC/NF only requires a low over-potential ($\eta_{50\ mA/cm2}$) of 220 mV for OER and 65 mV ($\eta_{10\ mA/cm2}$) for the HER; especially even at a large current density of 500 mA cm^{-2}, it requires only 296 mV for anodic oxidation. Additionally, when being used as a bifunctional catalyst for water splitting, the electrolyser only requires a low cell voltage of 1.47 and 1.70 V to obtain 10 and 50 mA cm^{-2}, respectively, for overall water splitting as well as extremely excellent durability for 100 h. The ultra-low cell voltage, large current density, and robust durability enable the Ni-Fe-P@NC/NF catalyst to be a highly promising candidate for industrial electrolyser application.

RESULTS AND DISCUSSION

Growth, Structure, and Morphology

Anion exchange durations were studied to obtain the critical condition where $NiMoO_4$ nanowires could be thoroughly transformed into $KNi[Fe(CN)_6]$. $[Fe(CN)_6]^{3-}$ has much stronger coordination toward Ni^{2+} than MoO_4^{2-} due to the lower solubility of $KNi[Fe(CN)_6]$ ($K_{sp(Co\text{-}PBA)} = 1.8*10^{-15}$) (Wang et al., 2019) compared with $NiMoO_4$ ($K_{sp} = 3.2*10^{-12}$) (Huang et al., 2014a), which is the driving force for the conversion. Figure 1A shows each unit cell contains four $KNi[Fe(CN)_6]$ molecules. Each $[Fe(CN)_6]^{3-}$ connects to six Ni atoms through cyanide bridges, and each Ni atom connects to the six nitrogen atoms of the six cyanide bridges. A face-centered cubic framework is formed from the Fe→ C≡N→ Ni linkages. Both Ni and Fe atoms are six-coordinated with octahedral geometry. K atoms occupy the vacancies of the unit cell. The formation of PBA hollow structure probably follows a pseudo Kirkendall effect (Figure 1B) involved in the anion exchange reaction of the solid $NiMoO_4$ nanowires with the $K_3[Fe(CN)_6]$ solution (Jin fan et al., 2006; Yin et al., 2004). The reaction took place in a way that the outward diffusion of Ni^{2+} from the $NiMoO_4$ core was faster than the inward diffusion of $[Fe(CN)_6]^{3-}$ toward the core crossed the $NiMoO_4/KNi[Fe(CN)_6]$ interface, which formed at the beginning of the reaction due to the lower solubility of PBA compared with $NiMoO_4$. The net effect was that all the Ni could move away from the center and get converted into $KNi[Fe(CN)_6]$, leaving a hollow core behind. The obtained materials are denoted as $NiMoO_4$@PBA-XX (XX means the PBA growth reaction duration). After the $NiMoO_4$/NF was immersed into a 25°mL vial at 90°C for 10 min ($NiMoO_4$@PBA-10min), the main diffraction peaks were still ascribed to $NiMoO_4$ (PDF No. 01-079-7562), whereas the characteristic peak at 20.1° belonging to $KNi[Fe(CN)_6]$ (PDF No. 01-089-8978) could also be observed in $NiMoO_4$@PBA-10min according to the XRD patterns (Figure S1). Compared with $NiMoO_4$@PBA-10min, the intensity of diffraction peaks assigning to $NiMoO_4$ decreased, whereas that from $KNi[Fe(CN)_6]$ increased in $NiMoO_4$@PBA-30min due to further growth of PBA. When the duration reaction time is further increased, characteristic peaks at 11.4° and 15.8° ascribed to $NiMoO_4$ were very weak in $NiMoO_4$@PBA-1h and finally disappeared in $NiMoO_4$@PBA-2h with only the peaks from $KNi[Fe(CN)_6]$, demonstrating a total conversion from $NiMoO_4$ to $KNi[Fe(CN)_6]$. The total conversion from $NiMoO_4$ to $KNi[Fe(CN)_6]$ was also proved by ICP-MS (Table S1) result that only 0.88% of Mo was detected from Ni-Fe-P@NC, which is ignorable.

The morphology of $NiMoO_4$@PBA changed with different durations of anion exchange. In $NiMoO_4$@PBA-10min, the surface of $NiMoO_4$ became rough with some small cubic PBA growing *in situ* (Figures S2A and S2B). Further increases to 30 min ($NiMoO_4$@PBA-30min), 1 h, and 2 h caused the diameter of the nanowire to become larger with obvious crystal structures along the nanowires (see Figures S2C–S2H). Specifically, in $NiMoO_4$@PBA-2h, a hollow structure was observed (Figure S2H).

In order to obtain electrocatalysts that are active for both HER and OER, $NiMoO_4$@PBA-2h nanotubes on nickel foams were further converted to Ni/Fe-based phosphides embedded in N-doped carbon through a low-temperature phosphidation. A hollow structure was found on the end of the Ni-Fe-P@NC nanotubes, circled in the SEM image (Figure 2A). The nano-tubular structure of Ni-Fe-P@NC was obviously displayed (Figure 2B), and the wall of the tube was composed of small nanoparticles that belonged to small Ni-Fe-P nanoparticles according to the high-magnification TEM images (Figure 2C). The lattice fringe of 0.19 nm is attributed to the (210) plane of Ni_2P (PDF 03-065-1989) or Fe_2P (PDF 00-033-0670), which is consistent with the strongest diffraction peak at 47.7° in XRD patterns (Figure S3). The other peaks were weak, suggesting a low crystallinity of Ni-Fe-P nanoparticles. The presence of weak and broad ring-like patterns (Figure 2B, **inset**) in selected area electron diffraction (SAED) further confirmed the low crystallinity of Ni-Fe-P@NC.

Scanning transmission electron microscopy (STEM) was also applied to study the elemental distribution along Ni-Fe-P@NC nanotube (Figure 2D), which showed successful incorporation of P into $NiMoO_4$@PBA-2h with uniform distribution along the nanotube. Because of a tendency to migrate together, Ni existed as small particles, whereas Fe was distributed more uniformly. C and N derived from CN group of $KNi[Fe(CN)_6]$ were distributed uniformly along the nanotube. The hollow structure of Ni-Fe-P@NC was further proven by the line scan spectrum (Figure S4), which showed a valley-like intensity profile across the tube diameter. The inside diameter of the Ni-Fe-P@NC nanotube was measured to be around 200 nm with a thickness of 45 nm. The size of Ni-Fe-P nanoparticles was below 20 nm. The pore size distribution of Ni-Fe-P@NC was measured to be 30–50 nm and 150–200 nm (Figure S5), which demonstrated that Ni-Fe-P@NC has hierarchical structures with meso- and macro-pores, resulting in the fast mass transfer during electrocatalytic process.

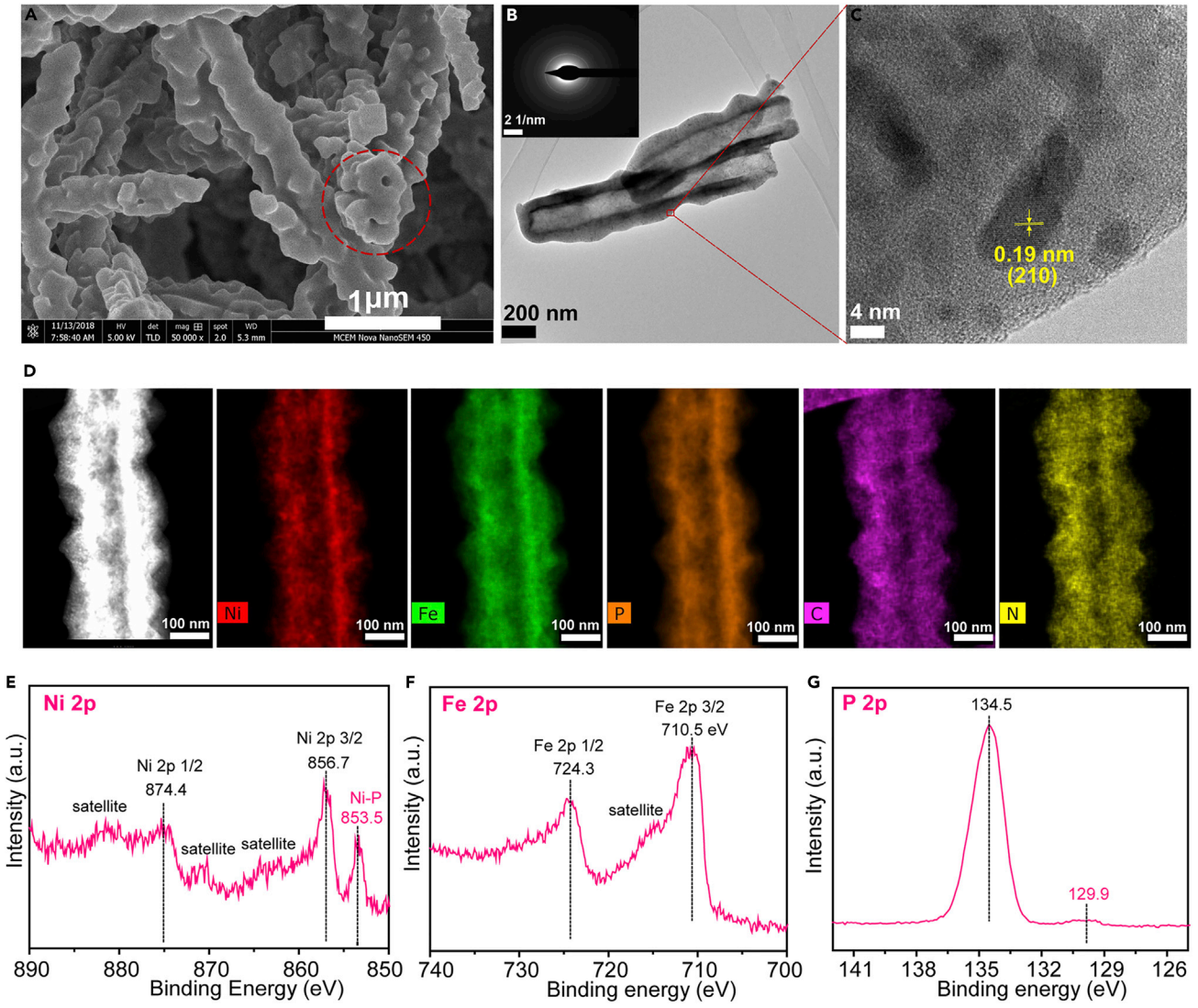

Figure 2. Characterization of the Ni-Fe-P@NC Nanotubes

(A–G) (A) SEM, (B) TEM images (inset: SAED pattern), and (C) high-magnification TEM images of Ni-Fe-P@NC porous nanotubes. (D) HAADF and elemental mapping of each element along the porous nanotube. Scale bars represent 100 nm. The XPS spectra Ni 2p (E), Fe 2p (F), and P 2p (G) of Ni-Fe-P porous nanotubes.

The surface chemical states of Ni-Fe-P@NC were also investigated by X-ray photoelectron spectroscopy (XPS) (Figures 2E–2G). The high-resolution Ni 2p XPS spectrum (Figure 2E) displayed two $2p_{3/2}$ (853.5 and 856.7 eV) and $2p_{1/2}$ (874.4 eV) doublets, together with broad satellites at higher binding energies (BEs). The lower BE doublet (853.5 eV) can be assigned to nickel phosphide, whereas the higher BE doublet most likely corresponds to mainly Ni hydroxide (Biesinger et al., 2009). In Fe 2p spectrum, two obvious peaks with satellite features were located at 724.3 and 710.5 eV, corresponding to Fe $2p_{1/2}$ and Fe $2p_{3/2}$, respectively (Figure 2F). The satellite peak around 715.0 eV was closer to Fe $2p_{3/2}$ rather than Fe $2p_{1/2}$, demonstrating a prevalence of Fe^{2+} in the catalyst with co-existence of Fe^{2+} and Fe^{3+} (Biesinger et al., 2011). No characteristic peak of iron phosphides was observed, suggesting the formation of Ni-Fe-P compound instead of a mixture of solid binary phases (Tang et al., 2016; Yu et al., 2017). Besides, the XPS spectrum of P 2p (Figure 2G) showed a peak at 129.9 eV, consistent with the nickel phosphide, whereas the peak at 134.5 eV can be assigned to that of metal phosphates or other phosphorous oxides species that might be originated from surface oxidation by air (Tang et al., 2016).

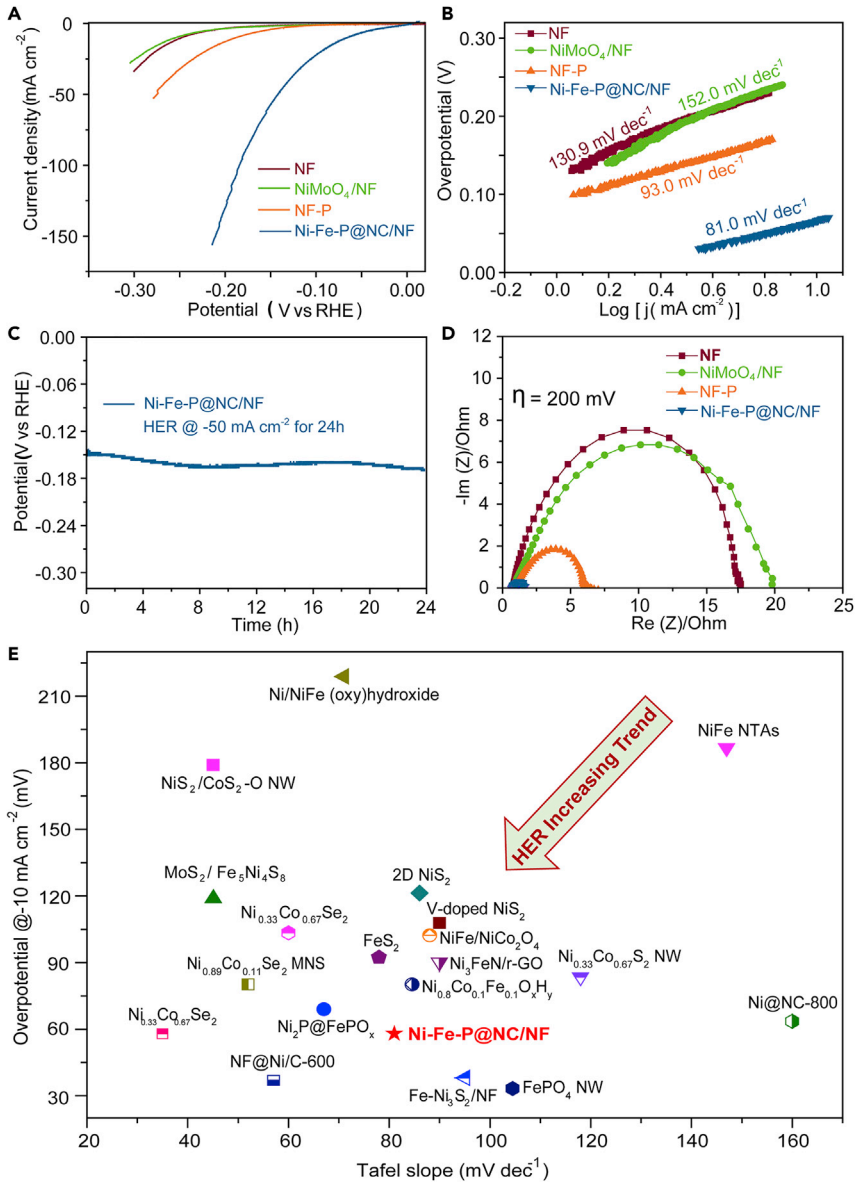

Figure 3. HER Performance in 1 M KOH

(A and B) (A) Linear sweep voltammetry (LSV) and (B) Tafel slope of Ni-Fe-P@NC/NF, $NiMoO_4$/NF, NF-P, and NF.

(C) Long-term electrolysis for HER of Ni-Fe-P@NC/NF at −50 mA cm^{-2} for 24 h.

(D) Nyquist plots at an over-potential of 200 mV for NF, $NiMoO_4$/NF, NF-P, and Ni-Fe-P@NC/NF.

(E) HER activity comparison with recently reported excellent Ni/Fe-based HER catalysts by plotting the curve of the over-potential at −10 mA cm^{-2} with Tafel slope (corresponding references seen in Table S3).

HER Performance of Ni-Fe-P@NC/NF

As $KNi[Fe(CN)_6]$ tends to be dissolved in strong alkaline solution based on the experiments carried out in 1.0 M KOH, it is ruled out as a control catalyst for electrocatalytic activity study. Ni-Fe-P@NC/NF exhibits a very small onset potential close to 0 mV *vs* RHE and a very low over-potential (η_{10}) of 66 mV to achieve a current density of 10 mA·cm^{-2}, whereas the substrate nickel foam (NF) and $NiMoO_4$/NF both have a low activity with η_{10} of 250 mV toward HER (Figure 3A). To exclude the effect from NF after phosphidation (NF-P), the HER performance of NF-P was also studied, which displayed a large over-potential of 190 mV to obtain a current density of 10 mA·cm^{-2}. In addition, Ni-Fe-P@NC/NF also showed higher HER performance than Ni_5P_4 and FeP (Figure S6), demonstrating the synergistic effects between Ni and Fe in the catalyst.

Compared with $NiMoO_4$ (152.0 mV•dec^{-1}), NF (130.9 mV•dec^{-1}), and NF-P (93.0 mV•dec^{-1}), the sample Ni-Fe-P@NC/NF has a lower Tafel slope of 81.0 mV•dec^{-1} (Figure 3B), demonstrating its fastest HER reaction rate among all the controlled catalysts reported in this work. According to the mechanism of hydrogen evolution, the HER process consists of two principal steps in alkaline electrolytes. The initial discharge step is called Volmer reaction ($H_2O + e- \rightarrow H_{ads} + OH^-$) with a high Tafel slope of 120 mV•dec^{-1}. Then, Heyrovsky reaction (the electrochemical desorption step): $H_{ads} + H_2O + e^- \rightarrow H_2 + OH^-$ or Tafel reaction (the recombination step): $H_{ads} + H_{ads} \rightarrow H_2$ happens with a relative lower Tafel slope of 40 and 30 mV•dec^{-1}, respectively. The Tafel slope of Ni-Fe-P@NC is 81.0 mV•dec^{-1}, which lies between 40 and 120 mV•dec^{-1}, suggesting that a Volmer-Heyrovsky mechanism might be responsible for the HER process in Ni-Fe-P@NC. The stability of Ni-Fe-P@NC/NF for HER is also excellent with only 20 mV increase after electrolysis at −50 mA•cm^{-2} for 24 h (Figure 3C). Besides, the Faradaic efficiency of Ni-Fe-P@NC/NF for HER was around 100%, indicating the high efficiency of conversion from electricity to H_2 (Figure S7). Such extraordinary HER performance enables Ni-Fe-P@NC nanotubes to rival other well-known NiFe-based catalysts (Figure 3E and Table S3), indicating that Ni-Fe-P@NC is among the most active alkaline HER catalysts.

To gain more insight into the HER activity of Ni-Fe-P@NC/NF, electrochemical impedance spectroscopy (EIS) was performed to study the HER kinetics in Ni-Fe-P@NC (Figure 3D). The EIS data of Ni-Fe-P@NC/NF is fitted by an equivalent circuit model that shows two semicircles (Figure S8). The semicircle at high frequency reflects the contact resistance between the nickel foam and Ni-Fe-P@NC, whereas the semicircle at middle and low frequency relates to the charge transfer at the interfaces between Ni-Fe-P@NC and electrolyte (Morales-Guio et al., 2016). The latter, i.e. charge transfer resistance (R_{ct}), is usually used to assess the kinetics of electrochemical process, and the smaller the R_{ct} reflects, the faster the kinetics, thus the larger the current density (Huang et al., 2014b). The results for the elements in the circuit are shown in Table S2. Ni-Fe-P@NC/NF displays the smallest diameter of the semicircle shown in the electrochemical impedance diagram (Figure 3D), which represents the smallest charge transfer resistance (~0.69 ohm) during HER process; in contrast the charge transfer resistance of NF, $NiMoO_4$/NF, and NF-P are 16.5, 19.1, and 5.1 ohm respectively. The favorable charge transfer of Ni-Fe-P@NC is ascribed to the conductive N-doped carbon, its hollow structure, and small active particles that expose more active sites for faster charge transfer.

The capacitances of the double layer at the solid-liquid interface for the samples were used to estimate the electrochemical surface areas (ECSA) and thus the rough amount of exposed active sites in the catalysts. The ECSA was calculated *via* cyclic voltammetry (CV) (Figure S9, calculation details shown in Supplemental Information). The double-layer capacitance (C_{dl}) of Ni-Fe-P@NC/NF was measured to be 687.9 mF•cm^{-2}, which was much higher than that of NF (3.1 mF•cm^{-2}), $NiMoO_4$/NF (3.8 mF•cm^{-2}), and NF-P (11.7 mF•cm^{-2}). The large C_{dl} (or ECSA) of Ni-Fe-P@NC/NF is attributed to the tubular nanowires, with small pores generated due to the release of CN and H_2O molecules during a low-temperature phosphidation process. Therefore, the large ECSA enables Ni-Fe-P@NC to expose more active sites toward HER with a high catalytic current density at low over-potentials. Furthermore, the heat treatment during the phosphidation process can facilitate the formation of N-doped nano-carbons derived from CN in PBA, thus protecting the obtained Ni-Fe-P nanoparticles from further aggregation or structure collapse during gas-generated HER process and ensuring an excellent stability of Ni-Fe-P@NC.

OER Performance of Ni-Fe-P@NC/NF

In addition to the high HER performance in alkaline solution, Ni-Fe-P@NC/NF also displays excellent OER performance (Figures 4A and 4B) in alkaline media with quite small over-potentials of 140, 220, and 260 mV to achieve 10, 50, and 100 mA• cm^{-2} (Table S4), respectively. In contrast, much larger over-potentials are needed for NF, $NiMoO_4$/NF, and NF-P to achieve 50 mA• cm^{-2} with 460, 320, and 350 mV, respectively. The oxidation peak at 1.35 V vs RHE observed for $NiMoO_4$/NF, and NF is ascribed to the redox process between Ni (II) and Ni (III). Ni-Fe-P@NC also exhibited much higher performance toward OER than FeP, with Ni_5P_4 showing the lowest OER activity among them (Figure S10). The Tafel slope of Ni-Fe-P@NC/NF is 84.6 mV·dec^{-1}, which is lower than that of NF (92.0 mV· dec^{-1}), $NiMoO_4$/NF (119.7 mV· dec^{-1}), and NF-P (203.0 mV· dec^{-1}), demonstrating more rapid OER rate achieved by using Ni-Fe-P@NC/NF electrocatalyst. Moreover, Ni-Fe-P@NC/NF also shows a robust durability for OER at 100 mA cm^{-2} with negligible performance degradation after electrolysis for 24 h (Figure 4C).

Electrochemical impedance spectroscopy (EIS) was also carried out to elucidate the charge transfer process during OER process. The Nyquist plot of Ni-Fe-P@NC/NF (Figure 4D) shows the smallest diameter

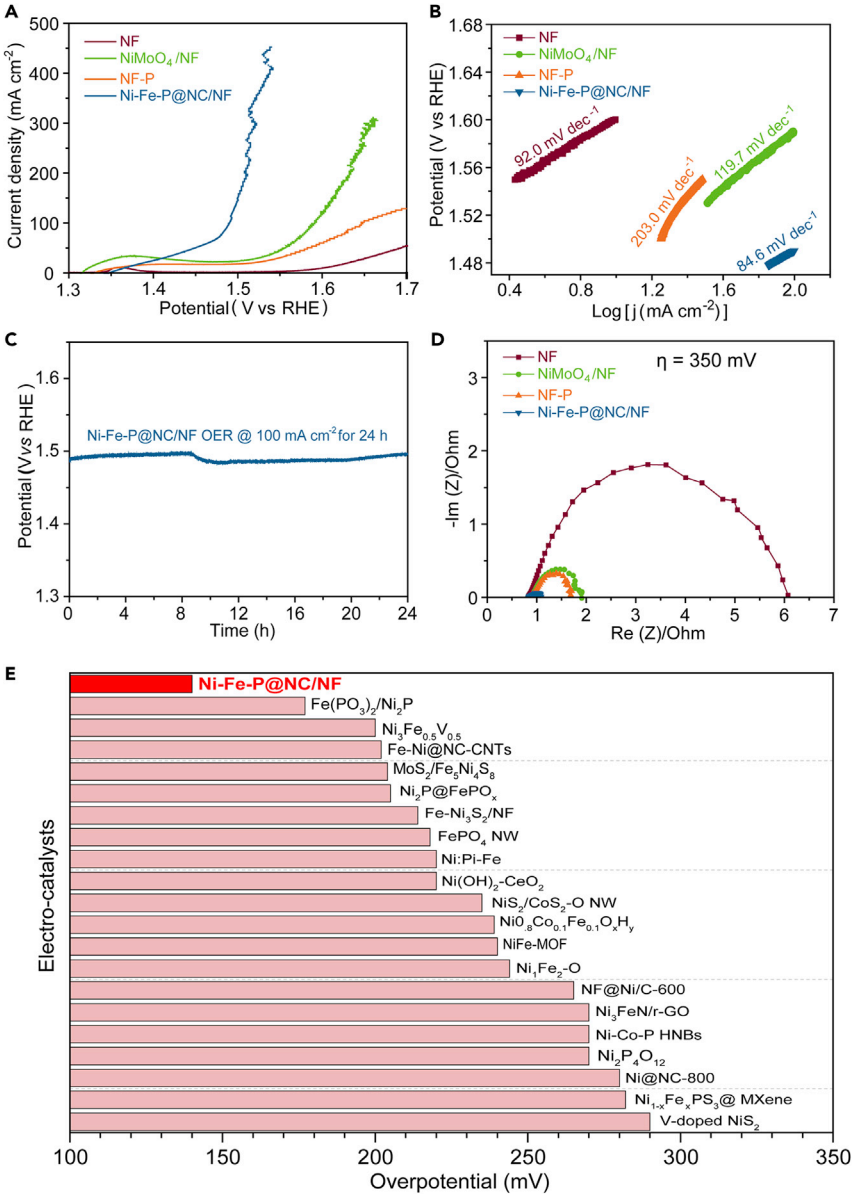

Figure 4. OER Performance in 1 M KOH

(A and B) (A) Linear sweep voltammetry (LSV) and (B) Tafel slope of Ni-Fe-P@NC/NF, $NiMoO_4$/NF, NF-P, and NF.

(C) Chronopoteniometric curve of Ni-Fe-P @NC/NF at 100 mA cm^{-2} for 24 h toward OER.

(D) Nyquist plots at an over-potential of 350 mV for NF, $NiMoO_4$/NF, NF-P, and Ni-Fe-P@NC/NF.

(E) Over-potential at 10 mA cm^{-2} of Ni-Fe-P@NC/NF comparison with recently reported excellent Ni/Fe-based OER catalysts (corresponding references seen in Table S4).

of the semicircle, corresponding to a charge transfer resistance of 0.2 ohm. In contrast, the charge transfer on NF, $NiMoO_4$/NF, and NF-P is much slow with a resistance of 5.5, 1.0, and 0.8 ohm, respectively. Therefore, Ni-Fe-P@NC/NF shows the most favorable charge transfer among all the controlled electrodes. The OER performance of Ni-Fe-P@NC/NF is comparable to those of the Ni/Fe-based catalysts reported previously in the literature, especially for its low over-potential at 10 mA· cm^{-2} (Figure 4E and Table S4).

Expectedly, Ni-Fe-P@NC/NF shows the highest C_{dl} of 5.6 mF·cm^{-2}, indicating the abundant active sites for OER, whereas the C_{dl} for NF, $NiMoO_4$/NF, and NF-P are calculated to be 1.9, 0.6, and 1.8 mF·cm^{-2}

(Figure S11). The high C_{dl} (or ECSA) of Ni-Fe-P@NC/NF is also derived from the hollow structure and the small size of Ni-Fe-P nanoparticles.

Commercial electrolysers require electrocatalysts to deliver high oxidative current densities (e.g. 500 mA cm^{-2}) at low over-potentials (e.g. 300 mV) over a long duration to well match the HER performance on the cathode (Lu and Zhao, 2015; Smith et al., 2013; Zhou et al., 2017). In our case, the Ni-Fe-P@NC/NF electrode only requires an over-potential of 296 mV to deliver a high current density of 500 mA·cm^{-2} (Figure S12), outperforming NF, $NiMoO_4$/NF, NF-P, and most of the NiFe-based electrocatalysts reported to date at high current densities. In addition, it is worth noting that although vigorous gas evolution occurs during electrolysis, gas bubbles dissipate rapidly into the solution and no bubbles are accumulated on the electrode surface due to the macro-structure of NF and the hollow structures of Ni-Fe-P@NC nanotubes.

Characterization and Analysis of Ni-Fe-P@NC after Electrolysis

To get into deep sight of the origins of its high HER and OER activity, Ni-Fe-P@NC/NF after HER and OER electrolysis were also studied. After HER electrolysis at −50 mA cm^{-2} for 24 h in alkaline solution, Ni-Fe-P nanotubes became fluffier than the original Ni-Fe-P nanotubes (Figure S14). Raman spectra obtained for Ni-Fe-P@NC/NF before and after HER/OER are presented (Figure S13). No obvious bands are observed on pristine nickel foam, which is consistent with its metallic nature. $NiMoO_4$/NF shows obvious peaks at 348, 845, 864, 897, and 948 cm^{-1}, ascribed to Mo-O vibration in $NiMoO_4$ (Frost et al., 2005; Han et al., 2015). Regarding $KNi[Fe(CN)_6]$/NF, a characteristic peak at 2,183 cm^{-1} belongs to Fe(III)-CN-Ni(II) vibration in $KNi[Fe(CN)_6]$ (Kettle et al., 2011). The bands below 500 cm^{-1} might be caused by Ni-P vibration in Ni_2P/NF. The fresh Ni-Fe-P@NC/NF shows two broad peaks located at 1,375 and 1,595 cm^{-1}, which belong to the D and G band of nano-carbons, respectively (He et al., 2017; Zhang et al., 2018a). A weak band at 680 cm^{-1} demonstrates the existence of Fe-O in Ni-Fe-P@NC/NF. After HER electrolysis at −50 mA cm^{-2} for 24 h, the D and G bands of nano-carbons can still be observed. However, due to the high pH environment, Ni and Fe oxy/hydroxides formed on the surface of Ni-Fe-P can lead to the generation of new peaks at 552 cm^{-1} ascribed to Ni-O and the peak at 675 cm^{-1} from the Fe-O vibrations of FeOOH (Shinagawa et al., 2017; Zou et al., 2017). XPS characterizations before and after HER (Figure S16) were also performed to understand the HER mechanism. After HER for 24 h, in the Ni 2p spectrum, the intensity of peaks at 8567.7 and 874.4 eV as well as their satellites enhances, whereas that of the peak at 853.5 eV belonging to nickel phosphide decreases, most likely due to the partial oxidation in aerobic environment (Zou et al., 2018). In Fe 2p spectrum, compared with the fresh Ni-Fe-P@NC catalyst, after HER electrolysis for 24 h, the peaks of Fe $2p_{3/2}$ and Fe $2p_{1/2}$ both shift to higher binding energies, with the satellite peak of Fe $2p_{3/2}$ shifting more closely toward Fe $2p_{1/2}$, indicating that more Fe^{3+} dominates in the catalyst after HER electrolysis. In the P 2p spectrum, the strength of the peak at 134.3 eV (mainly belonging to phosphates) reduces, which is in line with the phenomenon in Ni_2P reported by Wang and co-workers (Wang et al., 2016). With regard to the O 1s spectrum, fresh Ni-Fe-P@NC nanotubes have two distinct peaks located at 533.5 and 531.8 eV, mainly corresponding to oxygen in phosphate and surface hydroxides, respectively. After HER electrolysis, the peak at 533.5 eV reduces to a lower intensity, which is consistent with the changes in P 2p before and after the HER duration tests (Figure S16C) (Stoch and Gablankowska-Kukucz, 1991; Zhang et al., 2018c). After the HER duration test, the peak between 534.0 and 530.0 eV is probably assigned to hydroxides species, whereas the newly generated peak at 529.8 eV is ascribed to the metal oxide (Yu et al., 2016a).

After OER electrolysis at 100 mA cm^{-2} for 24 h, a new peak at 474 cm^{-1} is observed, and the other two peaks at 552 and 675 cm^{-1} are stronger than those after HER electrolysis. The peaks at 474 and 552 eV are ascribed to Ni-O vibrations in NiOOH, whereas the peak located at 675 cm^{-1} belongs to Fe-O in FeOOH, demonstrating that the real active sites in Ni-Fe-P@NC/NF for OER are NiOOH and FeOOH or Ni-Fe oxy/hydroxide (Shinagawa et al., 2017; Sun et al., 2017; Trześniewski et al., 2015).

The D and G bands belonging to nano-carbons disappear (Figure S13) as the high oxidation potential oxidized carbon into carbon oxides, in agreement with the mapping results that degradation of the nano-carbons occurs in Ni-Fe-P@NC/NF after OER electrolysis (Figure S15). Due to the positive potential, the *in-situ*-generated FeOOH shows as nano-sheets on the surface of Ni-Fe-P@NC based on the elemental mapping results (Figure S15) that Fe distributes along the nano-sheet, which is consistent with the Raman spectra analyzed above. The signal of P in Ni-Fe-P is strongly degraded after OER electrolysis for 24 h,

indicating that most of P is dissolved in the solution. The data show that Ni-Fe-P possibly experiences surface re-construction and is probably converted to a mixture of amorphous FeOOH nano-sheets and Ni-Fe oxy/hydroxide, which are the real active sites for robust catalytic performance to water oxidation. The similar surface re-construction and formation of new species also happen in $Fe(PO_3)_2$/Ni_2P and Ni_2P@$FePO_x$ (Zhang et al., 2018b; Zhou et al., 2017) and other transition-metal compounds (i.e. sulfides, selenides, phosphides, nitrides, carbides, or borides)-based electrocatalysts during OER process (Chen et al., 2015; Fabbri et al., 2017; Mabayoje et al., 2016; Wygant et al., 2018).

Furthermore, according to the XPS spectra before and after the OER test (Figure S16), the peak at 853.5 eV belonging to nickel phosphides in Ni 2p spectrum disappears, which is consistent with the Ni-P signal in P 2p (Figure S16C). The characteristic peaks in Fe 2p are both shifted to higher binding energies with the Fe $2p_{3/2}$ satellite peak shifting closer to Fe $2p_{1/2}$ compared with the sample before OER, suggesting that Fe^{3+} prevails in Ni-Fe-P after OER (Biesinger et al., 2011), which is possibly due to the oxidation of Fe during OER process. After OER, the P 2p peak vanishes due to a possible oxidation of phosphides into phosphates followed by a further dissolution in alkaline solutions. Only one broad peak with a range from 534.4 to 527.1 eV is observed in O 1s after OER, which probably includes the peaks belonging to hydroxides and newly generated nickel or iron oxide/hydroxide on the surface of the phosphides. These XPS results are in good agreement with that from Raman spectra as well as that reported by Zhou and co-workers (Zhou et al., 2017).

Overall Water Splitting

The bifunctional catalytic properties toward both HER and OER of Ni-Fe-P@NC/NF enable it to be used as both the cathode and anode for the build-up of a complete cell in 1.0 M KOH electrolyte. Not surprisingly, Ni-Fe-P@NC/NF-based alkaline electrolyser delivers a water-splitting current density of 10 and 50 mA• cm^{-2} at a voltage of only 1.47 and 1.70 V, respectively, which out-performs the benchmark Pt/C (–)//RuO_2 (+) couple and other control electrodes (Figure 5A). In addition, Ni-Fe-P@NC/NF-based electrolyser displays strong durability with negligible performance degradation after continuous electrolysis at 50 mA cm^{-2} for 100 h (Figure 5B). A large amount of H_2 and O_2 bubbles is released from the cathode and anode at high current densities, respectively (Figure 5B, **inset**). Remarkably, the ultralow cell voltage of Ni-Fe-P@NC/NF for water electrolyser is superior to those state-of-the-art bifunctional electrocatalysts (Figure 5C), demonstrating that this catalyst is among the best-performing overall water splitting electrocatalysts reported so far. Finally, the capability of Ni-Fe-P@NC catalyst for solar-energy-driven water splitting was also investigated by connecting to a commercial silicon photovoltaic device with a solar-to-hydrogen conversion efficiency of 4.0% (Figures S17 and S18). Therefore, in consideration of the activity and durability, Ni-Fe-P@NC/NF holds great promise for practical alkaline water electrolysis applications.

Factors for High Catalytic Performance

The state-of-the-art bifunctional catalytic activities of Ni-Fe-P@NC/NF can mainly be attributed to the following aspects: (1) the structure of the electrode (especially its hierarchical porous structure). The direct growth of catalysts on the nickel foam can enable the best ohmic contact and mechanical robustness between the Ni-Fe-P@NC catalyst and nickel foam support, forming a fully integrated catalyst for efficient OER under stringent high current density and strong gas evolution conditions, resulting in a small charge transfer from substrate to catalysts. In addition, macro-pores of nickel foams and the hollow channels of Ni-Fe-P@NC nanotubes can promote the fast mass and charge transfer as well as hydrogen or oxygen release from the catalysts, whereas nano-pores can ensure adequate contact between the catalysts and the electrolyte for exposing abundant active sites. (2) The low crystallinity of Ni-Fe-P nanoparticles. The randomly arranged Ni-Fe-P grains can offer more unsaturated atoms as active sites for the adsorption of reactants and thus accelerate the reaction rate. (3) The multi-functions of N-doped nano-carbons. The existence of N-doped nano-carbons can not only improve the conductivity of the nano-hybrids for an enhanced charge transfer but also protect the obtained Ni-Fe-P nanoparticles from aggregation during the annealing process (Jin et al., 2015; Pan et al., 2018). Nano-carbons doped with heteroatoms, especially the nitrogen atom that has a similar atomic size with the carbon atom, have favorable electronic structure toward electrocatalytic process such as OER, due to enhanced adsorption of intermediates at specific sites compared with pure carbons (Yan et al., 2018; Zhang et al., 2015). (4) Synergistic effect between Ni and Fe in Ni-Fe-P (Friebel et al., 2015; Li et al., 2018; Louie and Bell, 2013; Trotochaud et al., 2014). The synergistic effect between Fe and Ni can tune their electronic structures, which relates to the binding energies of the

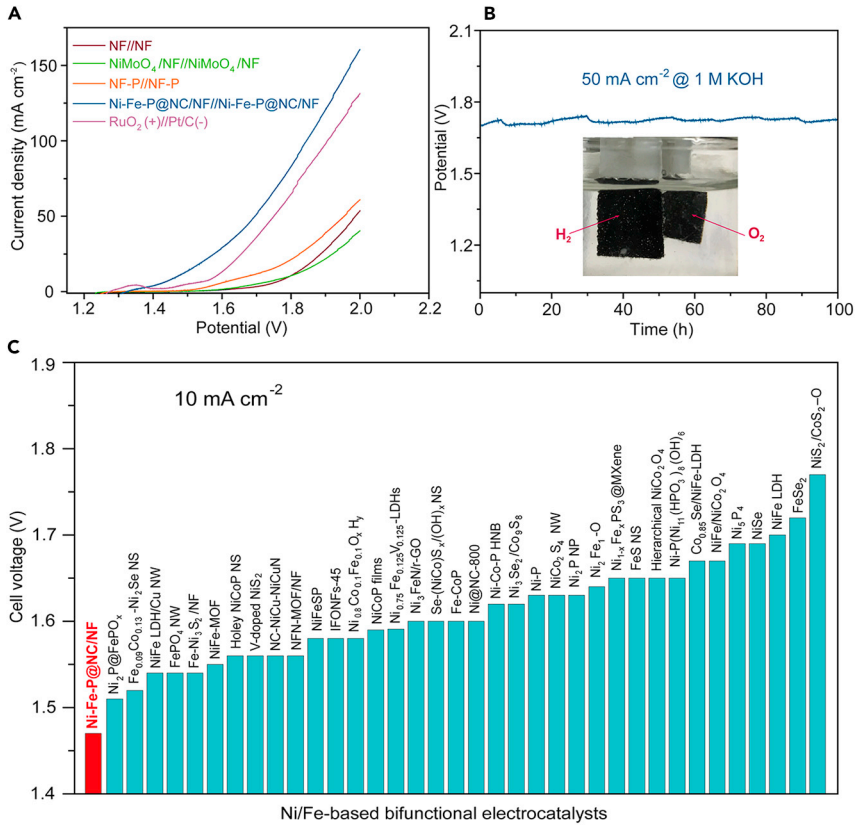

Figure 5. Overall Water Splitting Performance in 1 M KOH

(A) Polarization curves of Ni-Fe-P/NF//Ni-Fe-P/NF for overall water splitting at a scan rate of 5 mV s^{-1}.

(B) Chronopotentiometric curve of water electrolysis using Ni-Fe-P@NC/NF as both the anode and cathode at a constant current density of 50 mA cm^{-2} for 100 h (inset: hydrogen and oxygen are released from the cathode and anode, respectively).

(C) Comparison of the cell voltage to achieve 10 mA cm^{-2} among excellent Ni/Fe-based electrolysers ever reported (corresponding references seen in Table S5).

intermediates on the active sites of the catalysts (the intermediate in HER is hydrogen whereas those in OER are *OH, *O, and *OOH) during electrocatalytic process (Kibsgaard et al., 2015; Xiao et al., 2017).

Limitations of the Study

Our work has reported an effective bifunctional catalyst for both HER and OER, which can be assembled as an electrolyser with an ultralong stability. Although we have achieved high catalytic performance here, an in-depth understanding of the catalytic process still remains challenging. Therefore, in the near future, we will work on the catalytic process by some *in situ* characterizations as well as theoretical calculations.

METHODS

All methods can be found in the accompanying Transparent Methods supplemental file.

SUPPLEMENTAL INFORMATION

Supplemental Information can be found online at https://doi.org/10.1016/j.isci.2019.100761.

ACKNOWLEDGMENTS

This work is supported by the Australian Research Council through Discovery and Future Fellowship grants (Project No. DP160104089, FT140101256/Selomulya). We thank the financial support from the Monash University Postgraduate Publications Award (PPA). The help of Finlay Shanks in performing Raman analysis is

gratefully appreciated. We also acknowledge the use of facilities with the Monash Center for Electron Microscopy and ARC Funding (LE110100223). We thank the staff at the Monash Center for Electron Microscopy for their assistance with SEM and TEM characterization. We appreciate the help for XRD characterization and analysis from Jisheng Ma at the Monash X-ray platform. We also thank Tian Zhang for his help by setting up the silicon photovoltaic device for solar energy-driven water splitting test. We also appreciate the help for BET surface measurement and Faradaic efficiency test by Feifei Zhang and Yan Liang at Monash University, respectively.

AUTHOR CONTRIBUTIONS

Y.W, J.T., S.Z., and Y.Z. planned the study, designed the experiment, and analyzed the data. D.Z., J.T., and C.S. supervised the project. Y.W, S.Z., Y.Z., C.S., J.T., and D.Z. prepared the manuscript with input from all the other coauthors. All the authors reviewed and commented on the manuscript.

DECLARATION OF INTERESTS

The authors declare no competing interests.

Received: August 15, 2019
Revised: November 4, 2019
Accepted: December 5, 2019
Published: January 24, 2020

REFERENCES

Ahn, W., Park, M.G., Lee, D.U., Seo, M.H., Jiang, G., Cano, Z.P., Hassan, F.M., and Chen, Z. (2018). Hollow multivoid nanocuboids derived from ternary Ni–Co–Fe Prussian blue analog for dual-electrocatalysis of oxygen and hydrogen evolution reactions. Adv. Funct. Mater. *28*, 1802129.

Anandhababu, G., Huang, Y., Babu, D.D., Wu, M., and Wang, Y. (2018). Oriented growth of ZIF-67 to derive 2D porous CoPO nanosheets for electrochemical-/photovoltage-driven overall water splitting. Adv. Funct. Mater. *28*, 1706120.

Biesinger, M.C., Payne, B.P., Lau, L.W.M., Gerson, A., and Smart, R.S.C. (2009). X-ray photoelectron spectroscopic chemical state quantification of mixed nickel metal, oxide and hydroxide systems. Surf. Interface Anal. *41*, 324–332.

Biesinger, M.C., Payne, B.P., Grosvenor, A.P., Lau, L.W.M., Gerson, A.R., and Smart, R.S.C. (2011). Resolving surface chemical states in XPS analysis of first row transition metals, oxides and hydroxides: Cr, Mn, Fe, Co and Ni. Appl. Surf. Sci. *257*, 2717–2730.

Cai, G., Zhang, W., Jiao, L., Yu, S.-H., and Jiang, H.-L. (2017). Template-directed growth of well-aligned MOF arrays and derived self-supporting electrodes for water splitting. Chem *2*, 791–802.

Chen, W., Wang, H., Li, Y., Liu, Y., Sun, J., Lee, S., Lee, J.-S., and Cui, Y. (2015). In situ electrochemical oxidation tuning of transition metal disulfides to oxides for enhanced water oxidation. ACS Cent. Sci. *1*, 244–251.

de Tacconi, N.R., Rajeshwar, K., and Lezna, R.O. (2003). Metal Hexacyanoferrates: electrosynthesis, in situ characterization, and applications. Chem. Mater. *15*, 3046–3062.

Fabbri, E., Nachtegaal, M., Binninger, T., Cheng, X., Kim, B.-J., Durst, J., Bozza, F., Graule, T., Schäublin, R., Wiles, L., et al. (2017). Dynamic surface self-reconstruction is the key of highly active perovskite nano-electrocatalysts for water splitting. Nat. Mater. *16*, 925–931.

Fang, X., Jiao, L., Zhang, R., and Jiang, H.-L. (2017). Porphyrinic metal–organic framework-templated Fe–Ni–P/reduced graphene oxide for efficient electrocatalytic oxygen evolution. ACS Appl. Mater. Interfaces *9*, 23852–23858.

Friebel, D., Louie, M.W., Bajdich, M., Sanwald, K.E., Cai, Y., Wise, A.M., Cheng, M.-J., Sokaras, D., Weng, T.-C., Alonso-Mori, R., et al. (2015). Identification of highly active Fe sites in (Ni,Fe) OOH for electrocatalytic water splitting. J. Am. Chem. Soc. *137*, 1305–1313.

Frost, R.L., Musumeci, A.W., Martens, W.N., Adebajo, M.O., and Bouzaid, J. (2005). Raman spectroscopy of hydrotalcites with sulphate, molybdate and chromate in the interlayer. J. Raman Spectrosc. *36*, 925–931.

Ge, Y., Dong, P., Craig, S.R., Ajayan, P.M., Ye, M., and Shen, J. (2018). Transforming nickel hydroxide into 3D Prussian blue analogue array to obtain Ni2P/Fe2P for efficient hydrogen evolution reaction. Adv. Energy Mater. *8*, 1800484.

Han, N., Zhao, F., and Li, Y. (2015). Ultrathin nickel–iron layered double hydroxide nanosheets intercalated with molybdate anions for electrocatalytic water oxidation. J. Mater. Chem. A *3*, 16348–16353.

Han, L., Tang, P., Reyes-Carmona, Á., Rodríguez-García, B., Torréns, M., Morante, J.R., Arbiol, J., and Galan-Mascaros, J.R. (2016). Enhanced activity and acid pH stability of Prussian blue-type oxygen evolution electrocatalysts processed by chemical etching. J. Am. Chem. Soc. *138*, 16037–16045.

He, P., Yu, X.-Y., and Lou, X.W. (2017). Carbon-incorporated nickel–cobalt mixed metal phosphide nanoboxes with enhanced electrocatalytic activity for oxygen evolution. Angew. Chem. Int. Ed. *56*, 3897–3900.

Hou, Y., Wen, Z., Cui, S., Ci, S., Mao, S., and Chen, J. (2015). An advanced nitrogen-doped graphene/cobalt-embedded porous carbon polyhedron hybrid for efficient catalysis of oxygen reduction and water splitting. Adv. Funct. Mater. *25*, 872–882.

Huang, S., Zhao, Z., Chen, X., and Li, F. (2014a). Alkali extraction of valuable metals from spent Mo–Ni/Al2O3 catalyst. Int. J. Refract. Metals Hard Mater. *46*, 109–116.

Huang, Z., Chen, Z., Chen, Z., Lv, C., Humphrey, M.G., and Zhang, C. (2014b). Cobalt phosphide nanorods as an efficient electrocatalyst for the hydrogen evolution reaction. Nano Energy *9*, 373–382.

Jiao, L., Zhou, Y.-X., and Jiang, H.-L. (2016). Metal–organic framework-based CoP/reduced graphene oxide: high-performance bifunctional electrocatalyst for overall water splitting. Chem. Sci. *7*, 1690–1695.

Jin fan, H., Knez, M., Scholz, R., Nielsch, K., Pippel, E., Hesse, D., Zacharias, M., and Gösele, U. (2006). Monocrystalline spinel nanotube fabrication based on the Kirkendall effect. Nat. Mater. *5*, 627–631.

Jin, H., Wang, J., Su, D., Wei, Z., Pang, Z., and Wang, Y. (2015). In situ cobalt–cobalt oxide/N-doped carbon hybrids as superior bifunctional electrocatalysts for hydrogen and oxygen evolution. J. Am. Chem. Soc. *137*, 2688–2694.

Kettle, S.F.A., Diana, E., Marchese, E.M.C., Boccaleri, E., and Stanghellini, P.L. (2011). The vibrational spectra of the cyanide ligand revisited: the ν(CN) infrared and Raman spectroscopy of Prussian blue and its analogues. J. Raman Spectrosc. *42*, 2006–2014.

Kibsgaard, J., Tsai, C., Chan, K., Benck, J.D., Nørskov, J.K., Abild-Pedersen, F., and Jaramillo, T.F. (2015). Designing an improved transition metal phosphide catalyst for hydrogen evolution using experimental and theoretical trends. Energy Environ. Sci. *8*, 3022–3029.

Li, H., Chen, S., Zhang, Y., Zhang, Q., Jia, X., Zhang, Q., Gu, L., Sun, X., Song, L., and Wang, X. (2018). Systematic design of superaerophobic nanotube-array electrode comprised of transition-metal sulfides for overall water splitting. Nat. Commun. *9*, 2452.

Long, C., Li, X., Guo, J., Shi, Y., Liu, S., and Tang, Z. (2019a). Electrochemical reduction of CO2 over heterogeneous catalysts in aqueous solution: recent progress and perspectives. Small Methods *3*, 1800369.

Long, C., Wang, K., Shi, Y., Yang, Z., Zhang, X., Zhang, Y., Han, J., Bao, Y., Chang, L., Liu, S., and Tang, Z. (2019b). Tuning the electronic structure of PtRu bimetallic nanoparticles for promoting the hydrogen oxidation reaction in alkaline media. Inorg. Chem. Front. *6*, 2900–2905.

Louie, M.W., and Bell, A.T. (2013). An investigation of thin-film Ni–Fe oxide catalysts for the electrochemical evolution of oxygen. J. Am. Chem. Soc. *135*, 12329–12337.

Lu, X., and Zhao, C. (2015). Electrodeposition of hierarchically structured three-dimensional nickel–iron electrodes for efficient oxygen evolution at high current densities. Nat. Commun. *6*, 6616.

Mabayoje, O., Shoola, A., Wygant, B.R., and Mullins, C.B. (2016). The role of anions in metal chalcogenide oxygen evolution catalysis: electrodeposited thin films of nickel sulfide as "pre-catalysts". ACS Energy Lett. *1*, 195–201.

Masa, J., Weide, P., Peeters, D., Sinev, I., Xia, W., Sun, Z., Somsen, C., Muhler, M., and Schuhmann, W. (2016). Amorphous cobalt boride (Co2B) as a highly efficient nonprecious catalyst for electrochemical water splitting: oxygen and hydrogen evolution. Adv. Energy Mater. *6*, 1502313.

Morales-Guio, C.G., Liardet, L., and Hu, X. (2016). Oxidatively electrodeposited thin-film transition metal (Oxy)hydroxides as oxygen evolution catalysts. J. Am. Chem. Soc. *138*, 8946–8957.

Nai, J., Zhang, J., and Lou, X.W. (2018). Construction of single-crystalline Prussian blue analog hollow nanostructures with tailorable topologies. Chem *4*, 1967–1982.

Pan, Y., Sun, K., Liu, S., Cao, X., Wu, K., Cheong, W.-C., Chen, Z., Wang, Y., Li, Y., Liu, Y., et al. (2018). Core–shell ZIF-8@ZIF-67-derived CoP nanoparticle-embedded N-doped carbon nanotube hollow polyhedron for efficient overall water splitting. J. Am. Chem. Soc. *140*, 2610–2618.

Panda, C., Menezes, P.W., Walter, C., Yao, S., Miehlich, M.E., Gutkin, V., Meyer, K., and Driess, M. (2017). From a molecular 2Fe-2Se precursor to a highly efficient iron diselenide electrocatalyst for overall water splitting. Angew. Chem. Int. Ed. *56*, 10506–10510.

Shinagawa, T., Ng, M.T.-K., and Takanabe, K. (2017). Boosting the performance of the nickel anode in the oxygen evolution reaction by simple electrochemical activation. Angew. Chem. *129*, 5143–5147.

Smith, R.D.L., Prévot, M.S., Fagan, R.D., Zhang, Z., Sedach, P.A., Siu, M.K.J., Trudel, S., and Berlinguette, C.P. (2013). Photochemical route for accessing amorphous metal oxide materials for water oxidation catalysis. Science *340*, 60–63.

Stoch, J., and Gablankowska-Kukucz, J. (1991). The effect of carbonate contaminations on the XPS O 1s band structure in metal oxides. Surf. Interface Anal. *17*, 165–167.

Sun, H., Xu, X., Yan, Z., Chen, X., Cheng, F., Weiss, P.S., and Chen, J. (2017). Porous multishelled Ni2P hollow microspheres as an active electrocatalyst for hydrogen and oxygen evolution. Chem. Mater. *29*, 8539–8547.

Tang, C., Gan, L., Zhang, R., Lu, W., Jiang, X., Asiri, A.M., Sun, X., Wang, J., and Chen, L. (2016). Ternary FexCo1–xP nanowire array as a robust hydrogen evolution reaction electrocatalyst with Pt-like activity: experimental and theoretical insight. Nano Lett. *16*, 6617–6621.

Trotochaud, L., Young, S.L., Ranney, J.K., and Boettcher, S.W. (2014). Nickel–iron oxyhydroxide oxygen-evolution electrocatalysts: the role of intentional and incidental iron incorporation. J. Am. Chem. Soc. *136*, 6744–6753.

Trześniewski, B.J., Diaz-Morales, O., Vermaas, D.A., Longo, A., Bras, W., Koper, M.T.M., and Smith, W.A. (2015). In situ observation of active oxygen species in Fe-containing Ni-based oxygen evolution catalysts: the effect of pH on electrochemical activity. J. Am. Chem. Soc. *137*, 15112–15121.

Wang, X., Li, W., Xiong, D., Petrovykh, D.Y., and Liu, L. (2016). Bifunctional nickel phosphide nanocatalysts supported on carbon fiber paper for highly efficient and stable overall water splitting. Adv. Funct. Mater. *26*, 4067–4077.

Wang, Y., Ma, J., Wang, J., Chen, S., Wang, H., and Zhang, J. (2019). Interfacial scaffolding preparation of hierarchical PBA-based derivative electrocatalysts for efficient water splitting. Adv. Energy Mater. *9*, 1802939.

Wu, H.B., Xia, B.Y., Yu, L., Yu, X.-Y., and Lou, X.W. (2015). Porous molybdenum carbide nano-octahedrons synthesized via confined carburization in metal-organic frameworks for efficient hydrogen production. Nat. Commun. *6*, 6512.

Wygant, B.R., Kawashima, K., and Mullins, C.B. (2018). Catalyst or precatalyst? The effect of oxidation on transition metal carbide, pnictide, and chalcogenide oxygen evolution catalysts. ACS Energy Lett. *3*, 2956–2966.

Xiao, X., He, C.-T., Zhao, S., Li, J., Lin, W., Yuan, Z., Zhang, Q., Wang, S., Dai, L., and Yu, D. (2017). A general approach to cobalt-based homobimetallic phosphide ultrathin nanosheets for highly efficient oxygen evolution in alkaline media. Energy Environ. Sci. *10*, 893–899.

Yan, P., Liu, J., Yuan, S., Liu, Y., Cen, W., and Chen, Y. (2018). The promotion effects of graphitic and pyridinic N combinational doping on graphene for ORR. Appl. Surf. Sci. *445*, 398–403.

Yin, Y., Rioux, R.M., Erdonmez, C.K., Hughes, S., Somorjai, G.A., and Alivisatos, A.P. (2004). formation of hollow nanocrystals through the nanoscale Kirkendall effect. Science *304*, 711–714.

Yin, H., Zhao, S., Zhao, K., Muqsit, A., Tang, H., Chang, L., Zhao, H., Gao, Y., and Tang, Z. (2015). Ultrathin platinum nanowires grown on single-layered nickel hydroxide with high hydrogen evolution activity. Nat. Commun. *6*, 6430.

Yin, J., Li, Y., Lv, F., Lu, M., Sun, K., Wang, W., Wang, L., Cheng, F., Li, Y., Xi, P., and Guo, S. (2017). Oxygen vacancies dominated NiS2/CoS2 interface porous nanowires for portable Zn–air batteries driven water splitting devices. Adv. Mater. *29*, 1704681.

Yu, X.-Y., Feng, Y., Guan, B., Lou, X.W., and Paik, U. (2016a). Carbon coated porous nickel phosphides nanoplates for highly efficient oxygen evolution reaction. Energy Environ. Sci. *9*, 1246–1250.

Yu, X.-Y., Feng, Y., Jeon, Y., Guan, B., Lou, X.W., and Paik, U. (2016b). Formation of Ni–Co–MoS2 nanoboxes with enhanced electrocatalytic activity for hydrogen evolution. Adv. Mater. *28*, 9006–9011.

Yu, J., Cheng, G., and Luo, W. (2017). Hierarchical NiFeP microflowers directly grown on Ni foam for efficient electrocatalytic oxygen evolution. J. Mater. Chem. A *5*, 11229–11235.

Zhang, J., Zhao, Z., Xia, Z., and Dai, L. (2015). A metal-free bifunctional electrocatalyst for oxygen reduction and oxygen evolution reactions. Nat. Nanotechnol. *10*, 444–452.

Zhang, G., Wang, G., Liu, Y., Liu, H., Qu, J., and Li, J. (2016a). Highly active and stable catalysts of phytic acid-derivative transition metal phosphides for full water splitting. J. Am. Chem. Soc. *138*, 14686–14693.

Zhang, Y., Ouyang, B., Xu, J., Chen, S., Rawat, R.S., and Fan, H.J. (2016b). 3D porous hierarchical nickel–molybdenum nitrides synthesized by RF plasma as highly active and stable hydrogen-evolution-reaction electrocatalysts. Adv. Energy Mater. *6*, 1600221.

Zhang, B., Lui, Y.H., Gaur, A.P.S., Chen, B., Tang, X., Qi, Z., and Hu, S. (2018a). Hierarchical FeNiP@ultrathin carbon nanoflakes as alkaline oxygen evolution and acidic hydrogen evolution catalyst for efficient water electrolysis and organic decomposition. ACS Appl. Mater. Interfaces *10*, 8739–8748.

Zhang, F.-S., Wang, J.-W., Luo, J., Liu, R.-R., Zhang, Z.-M., He, C.-T., and Lu, T.-B. (2018b). Extraction of nickel from NiFe-LDH into Ni2P@NiFe hydroxide as a bifunctional electrocatalyst for efficient overall water splitting. Chem. Sci. *9*, 1375–1384.

Zhang, Y., Gao, L., Hensen, E.J.M., and Hofmann, J.P. (2018c). Evaluating the stability of Co2P electrocatalysts in the hydrogen evolution reaction for both acidic and alkaline electrolytes. ACS Energy Lett. *3*, 1360–1365.

Zhao, S., Yin, H., Du, L., He, L., Zhao, K., Chang, L., Yin, G., Zhao, H., Liu, S., and Tang, Z. (2014). Carbonized nanoscale metal–organic

frameworks as high performance electrocatalyst for oxygen reduction reaction. ACS Nano *8*, 12660–12668.

Zhao, S., Wang, Y., Dong, J., He, C.-T., Yin, H., An, P., Zhao, K., Zhang, X., Gao, C., Zhang, L., et al. (2016). Ultrathin metal–organic framework nanosheets for electrocatalytic oxygen evolution. Nat. Energy *1*, 16184.

Zheng, Y., Cheng, P., Xu, J., Han, J., Wang, D., Hao, C., Alanagh, H.R., Long, C., Shi, X., and Tang, Z. (2019). MOF-derived nitrogen-doped nanoporous carbon for electroreduction of CO2 to CO: the calcining temperature effect and the mechanism. Nanoscale *11*, 4911–4917.

Zhou, H., Yu, F., Sun, J., He, R., Chen, S., Chu, C.-W., and Ren, Z. (2017). Highly active catalyst derived from a 3D foam of $Fe(PO_3)_2/Ni_2P$ for extremely efficient water oxidation. Proc. Natl. Acad. Sci. U S A *114*, 5607–5611.

Zhu, Y., Tahini, H.A., Hu, Z., Dai, J., Chen, Y., Sun, H., Zhou, W., Liu, M., Smith, S.C., Wang, H., and Shao, Z. (2019a). Unusual synergistic effect in layered Ruddlesden−Popper oxide enables ultrafast hydrogen evolution. Nat. Commun. *10*, 149.

Zhu, Y., Tahini, H.A., Wang, Y., Lin, Q., Liang, Y., Doherty, C.M., Liu, Y., Li, X., Lu, J., Smith, S.C., et al. (2019b). Pyrite-type ruthenium disulfide with tunable disorder and defects enables ultra-efficient overall water splitting. J. Mater. Chem. A *7*, 14222–14232.

Zou, X., Liu, Y., Li, G.-D., Wu, Y., Liu, D.-P., Li, W., Li, H.-W., Wang, D., Zhang, Y., and Zou, X. (2017). Ultrafast formation of amorphous bimetallic hydroxide films on 3D conductive sulfide nanoarrays for large-current-density oxygen evolution electrocatalysis. Adv. Mater. *29*, 1700404.

Zou, X., Wu, Y., Liu, Y., Liu, D., Li, W., Gu, L., Liu, H., Wang, P., Sun, L., and Zhang, Y. (2018). In situ generation of bifunctional, efficient Fe-based catalysts from mackinawite iron sulfide for water splitting. Chem *4*, 1139–1152.

ISCI, Volume *23*

Supplemental Information

Three-Dimensional Hierarchical Porous Nanotubes Derived from Metal-Organic Frameworks for Highly Efficient Overall Water Splitting

Yang Wang, Shenlong Zhao, Yinlong Zhu, Ruosang Qiu, Thomas Gengenbach, Yue Liu, Lianhai Zu, Haiyan Mao, Huanting Wang, Jing Tang, Dongyuan Zhao, and Cordelia Selomulya

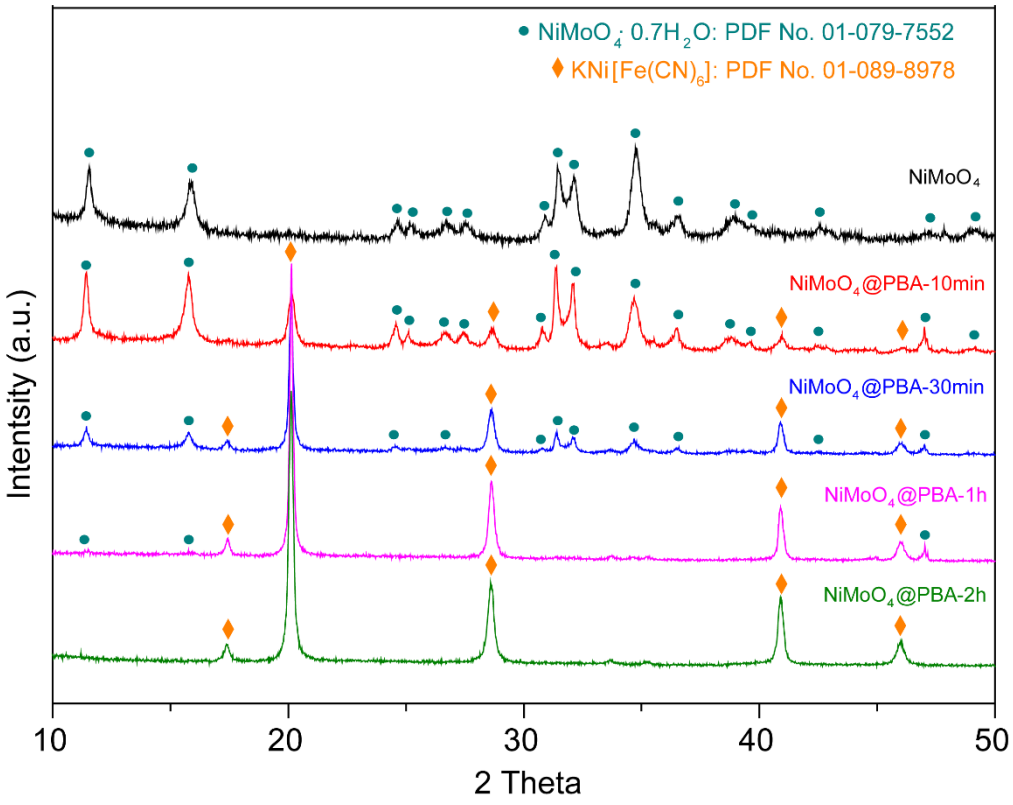

Figure S1. XRD patterns of $NiMoO_4$, $NiMoO_4$@PBA-10 min, $NiMoO_4$@PBA-30 min, $NiMoO_4$@PBA-1 h and $NiMoO_4$@PBA-2 h, related to **Figure 1**.

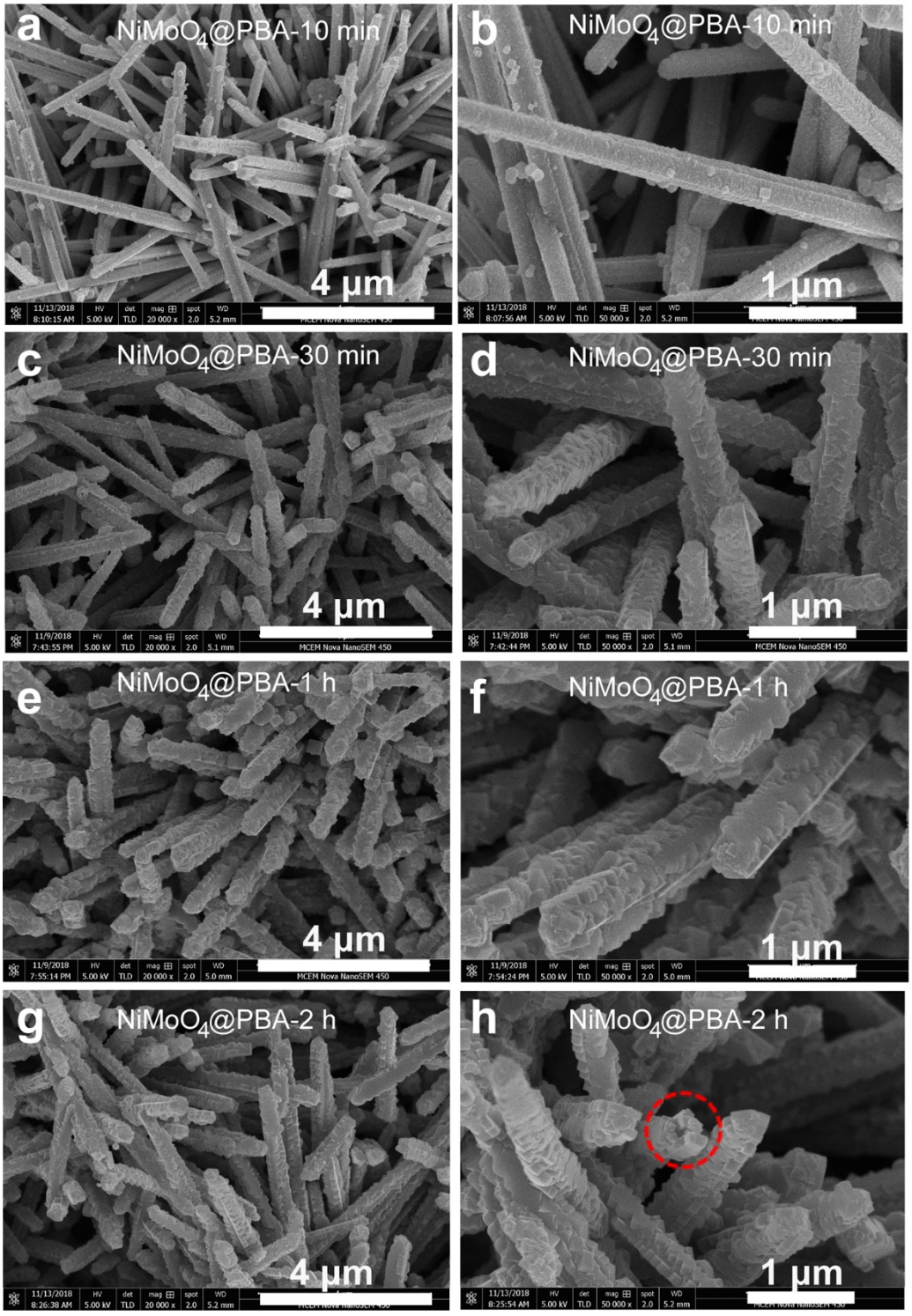

Figure S2. SEM images of $NiMoO_4$@PBA-10 min (a, b), $NiMoO_4$@PBA-30 min (c, d), $NiMoO_4$@PBA-1 h (e, f) and $NiMoO_4$@PBA-2 h (g, h) , related to **Figure 1**.

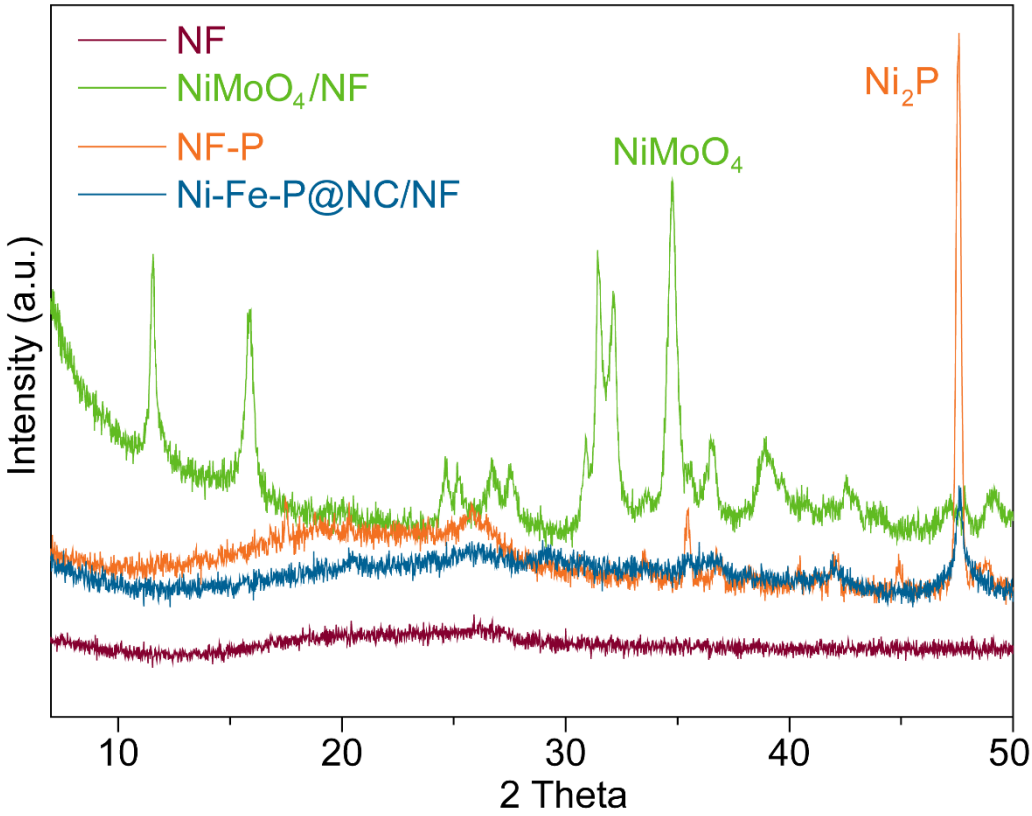

Figure S3. XRD patterns of Ni-Fe-P@NC/NF, $NiMoO_4$/NF, NF after phosphidation and original NF, related to **Figure 2**.

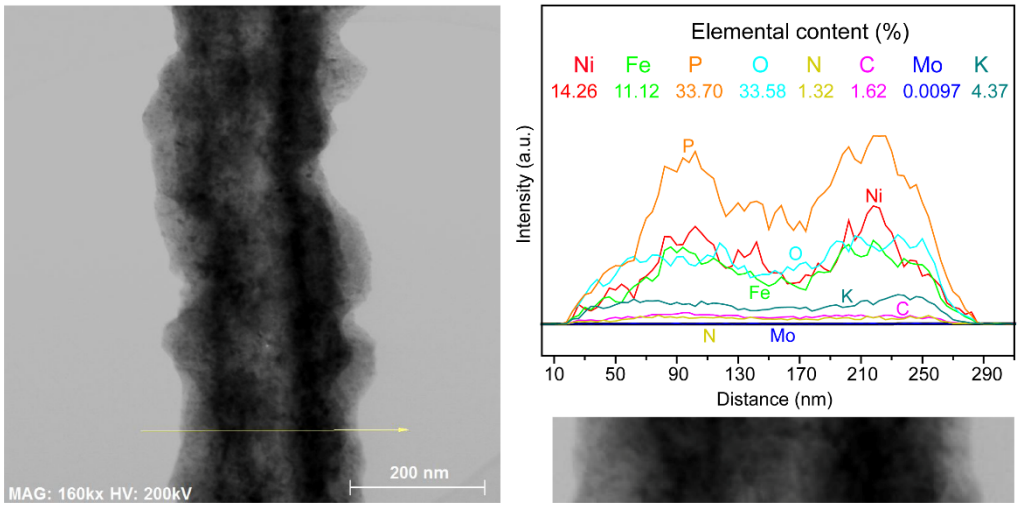

Figure S4. Line scan of Ni-Fe-P@NC nanotube and the elemental distribution on a radial direction, related to **Figure 2**.

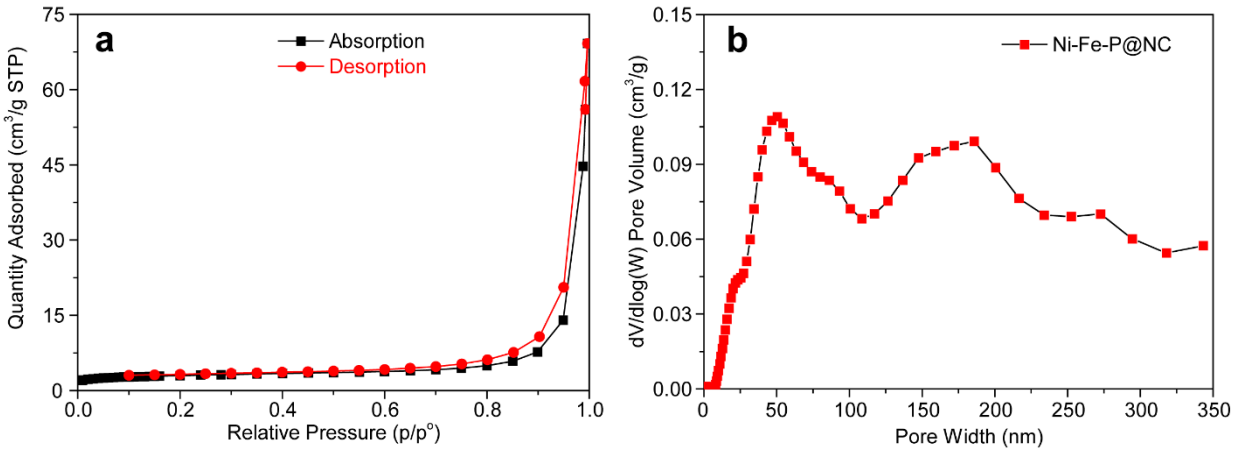

Figure S5. (**a**) N_2 adsorption-desorption isotherms and (**b**) corresponding pore size distribution plots of Ni-Fe-P@NC, related to **Figure 2**.

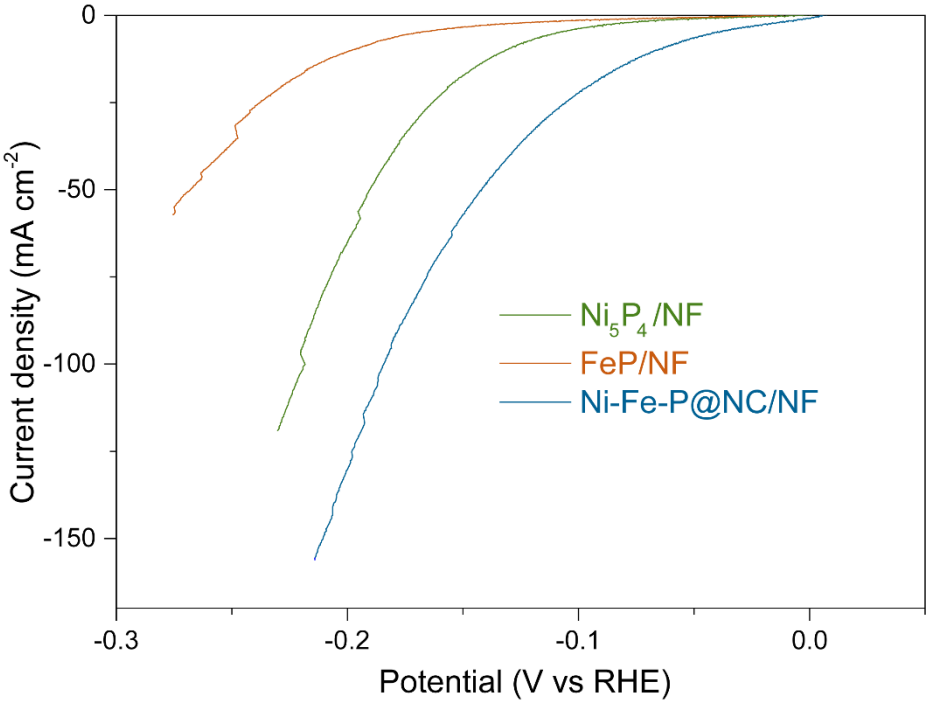

Figure S6. Linear sweep voltammetry (LSV) for HER comparison among Ni-Fe-P@NC/NF, Ni_5P_4 and FeP, related to **Figure 3**.

Faradaic efficiency

The Faradaic efficiency of hydrogen evolution reaction (FE_{HER}) was calculated based on the equation: $FE_{HER}= n_{H2} *2*F/ Q*100\%$

where n_{H2} was the amount of H_2 generated from HER, F was Faradaic constant and Q was the total charge applied on the working electrode.

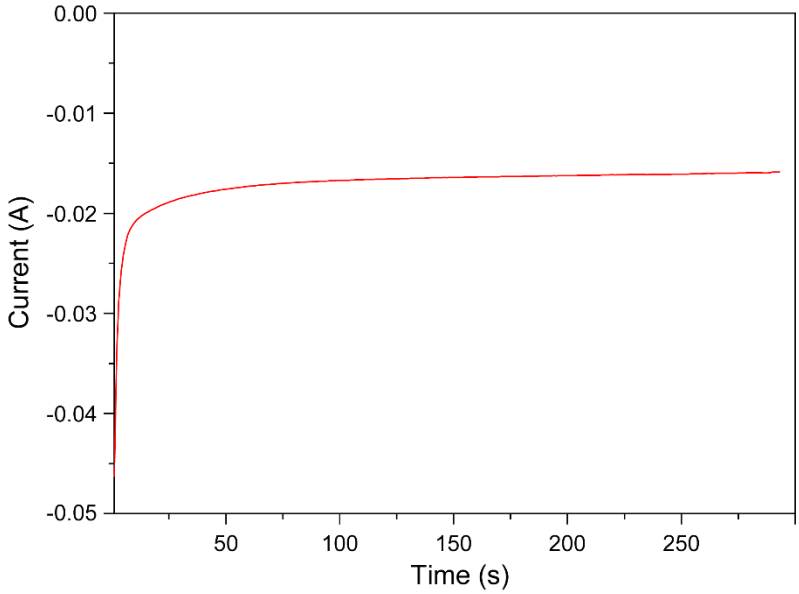

Figure S7. Chronoamperometric curves of Ni-Fe-P@NC/NF obtained at -0.1 V vs RHE for quantification of hydrogen, related to **Figure 3**.

When 5C of charge passed through the working electrode, the amount of obtained H_2 was detected by GC, which was 25.2 μmol. As there is systematic error including the relatively sealed electrochemical cell which might release H_2 during the transport to the GC, the error bar is around ± 3%.

$FE_{HER}= (25.2*10^{-6}$ mol*2*96485 C·mol$^{-1})$/5C*100%= 97.3% ± 3%

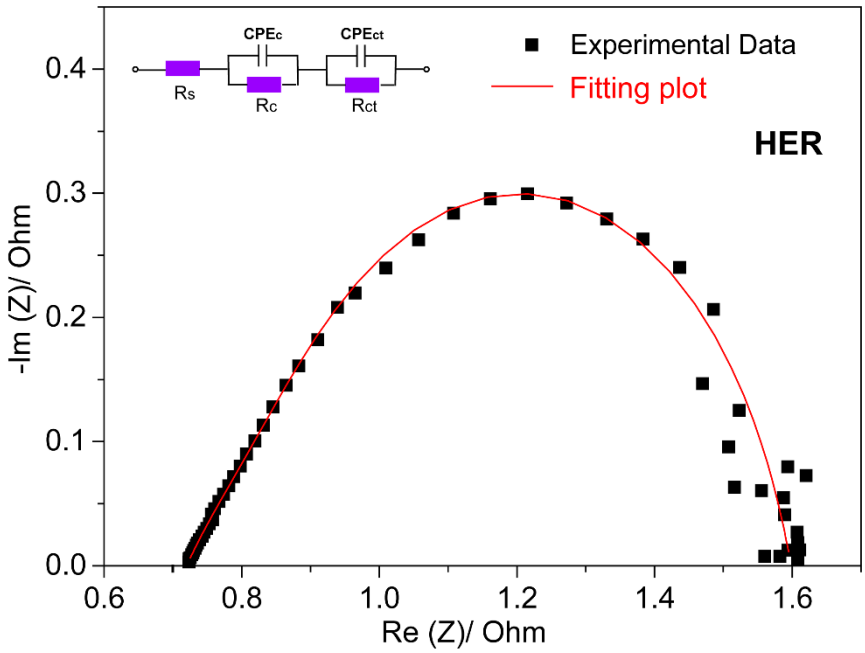

Figure S8. EIS Nyquist plots of Ni-Fe-P@NC/NF; inset: the corresponding equivalent circuit diagram, related to **Figure 3**.

R_s is the uncompensated solution resistance, CPE_c and R_c are the constant element and resistance reflecting electron transport at the interface between Ni-Fe-P@NC and NF, respectively. CPE_{ct} and R_{ct} are the constant phase element and charge transfer resistance at the Ni-Fe-P/electrolyte interface, respectively.

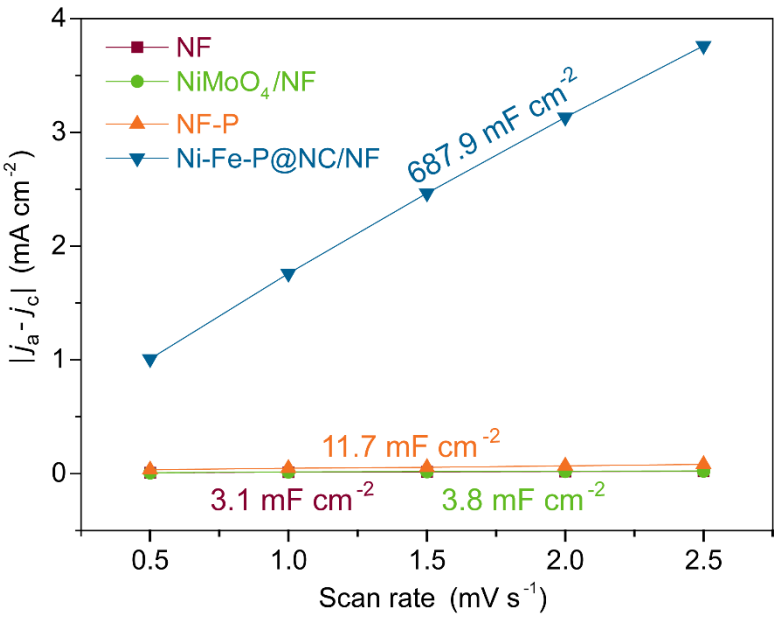

Figure S9. Plot showing the extraction of the double-layer capacitance (C_{dl}) for NF, $NiMoO_4$/NF, NF-P and Ni-Fe-P@NC/NF at -0.85 V *vs* Hg/HgO, related to **Figure 3**.

Normally, the specific capacitance for 1 cm^2 of a flat surface is around 20-60 $\mu F \cdot cm^{-2}$ and the average value of 40 $\mu F \cdot cm^{-2}$ is generally used for calculations. The specific capacitance can be obtained from geometric current density collected from the rectangular CV plots at a certain potential of -0.85 V *vs* Hg/HgO with a sweep rate from 0.5 to 2.5 mV s^{-1}.

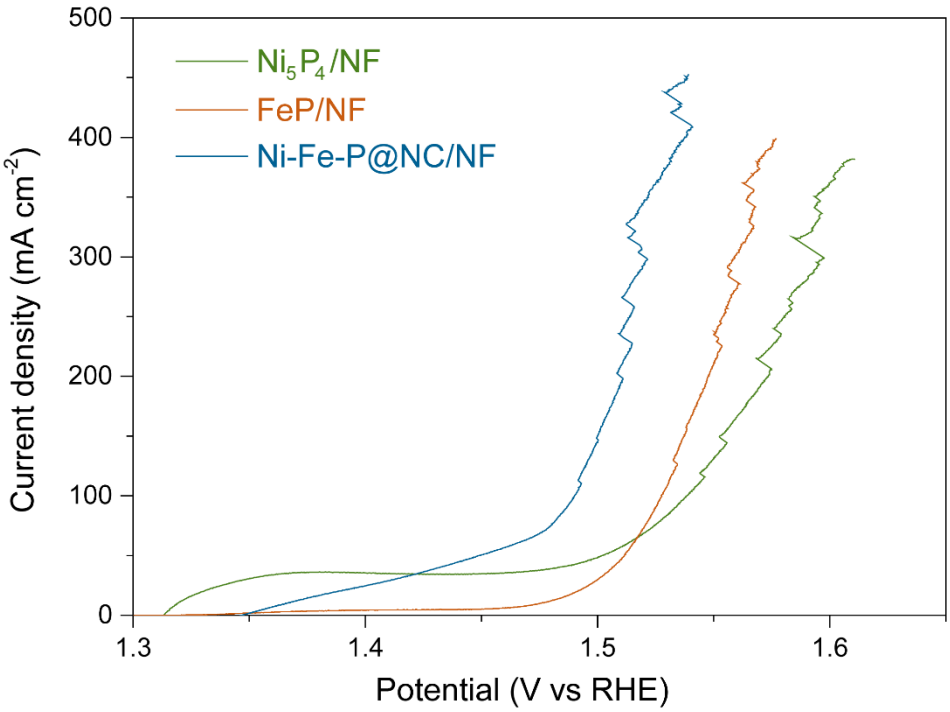

Figure S10. Linear sweep voltammetry (LSV) for OER comparison among Ni-Fe-P@NC/NF, Ni_5P_4 and FeP, related to **Figure 4**.

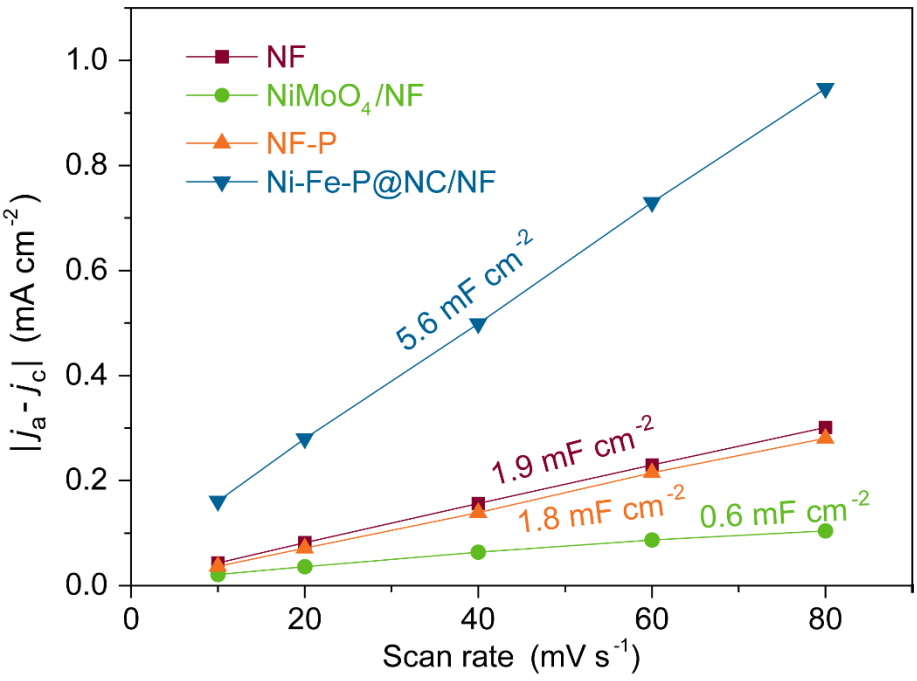

Figure S11. Plot showing the extraction of the double-layer capacitance (C_{dl}) for NF, $NiMoO_4$/NF, NF-P and Ni-Fe-P@NC/NF at 0.15 V *vs* Hg/HgO based on the CV curves at different scan rates with a potential range of 0.1~ 0.2 V *vs* Hg/HgO, related to **Figure 4**.

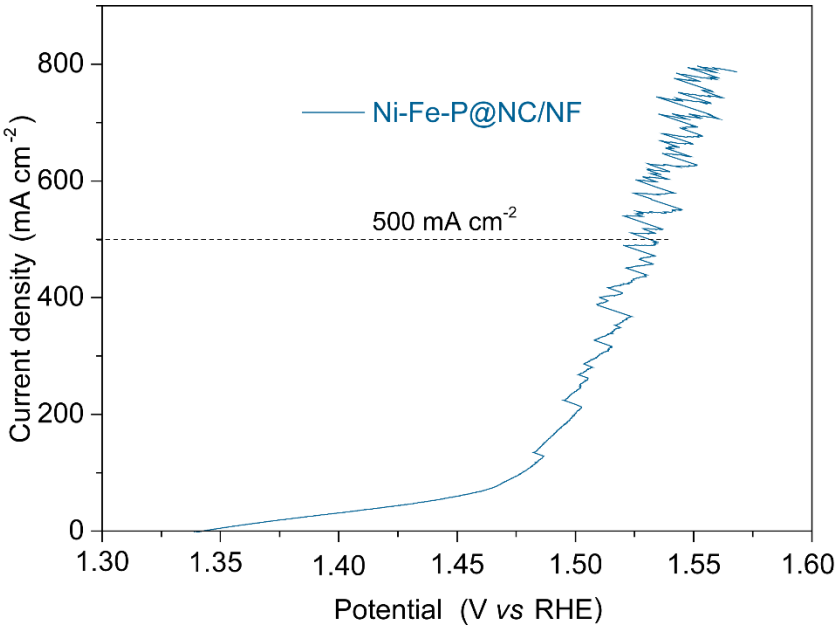

Figure S12. Linear sweep voltammetry (LSV) of Ni-Fe-P@NC/NF at higher potential LSV (500 mA cm^{-2} at 296 mV), related to **Figure 4**.

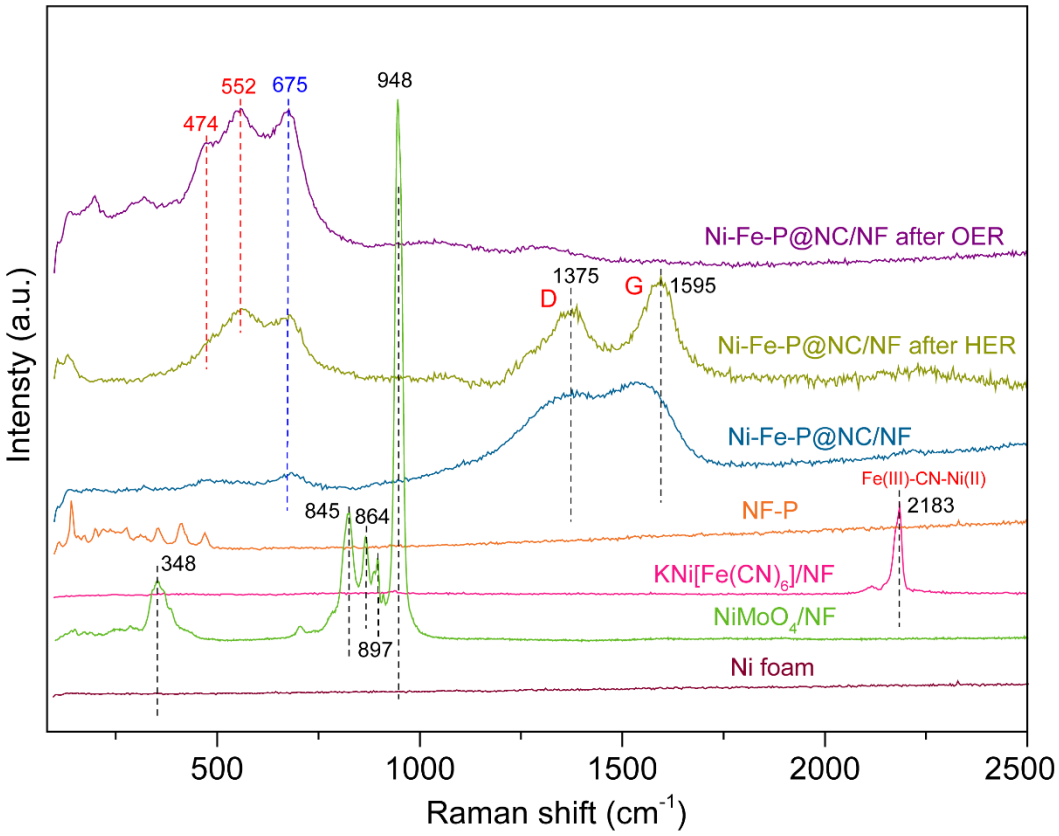

Figure S13. Raman spectra of Ni foam, $NiMoO_4$/NF, $KNi[Fe(CN)_6]$/NF, Ni-Fe-P@NC/NF, Ni-Fe-P@NC/NF after HER and Ni-Fe-P@NC/NF after OER, related to **Figure 2, 3 & 4**.

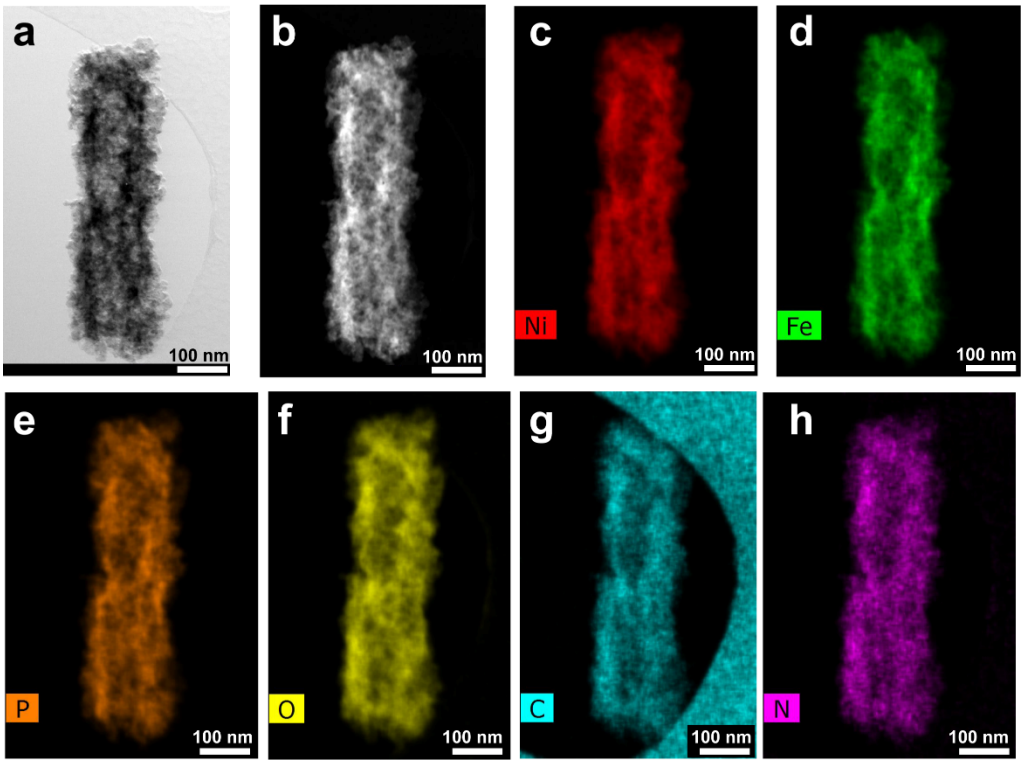

Figure S14. BF_DF (a), HAADF (b) and elemental mapping of each element (c-h) along the Ni-Fe-P@NC nanotube after HER at -50 mA cm^{-2} for 24 h. Scale bars are 100 nm, related to **Figure 3**.

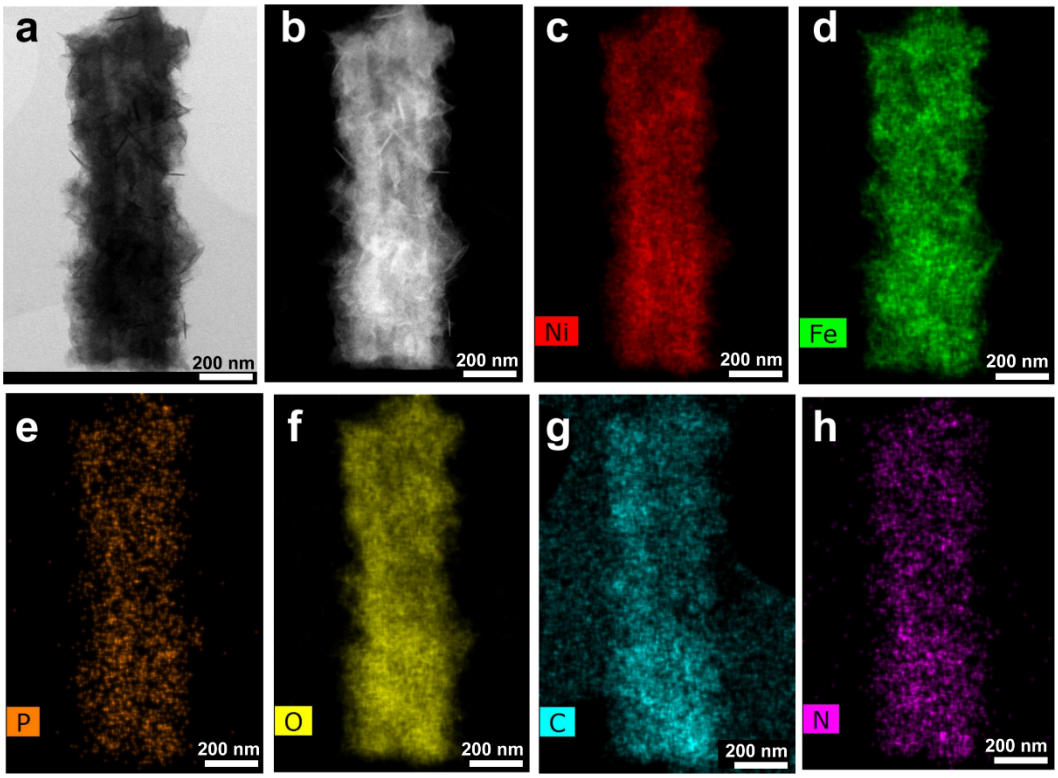

Figure S15. BF_DF (a), HAADF (b) and elemental mapping of each elements (c-h) along the Ni-Fe-P@NC nanotube after OER at 100 mA cm^{-2} for 24 h. Scale bars are 200 nm, related to **Figure 4**.

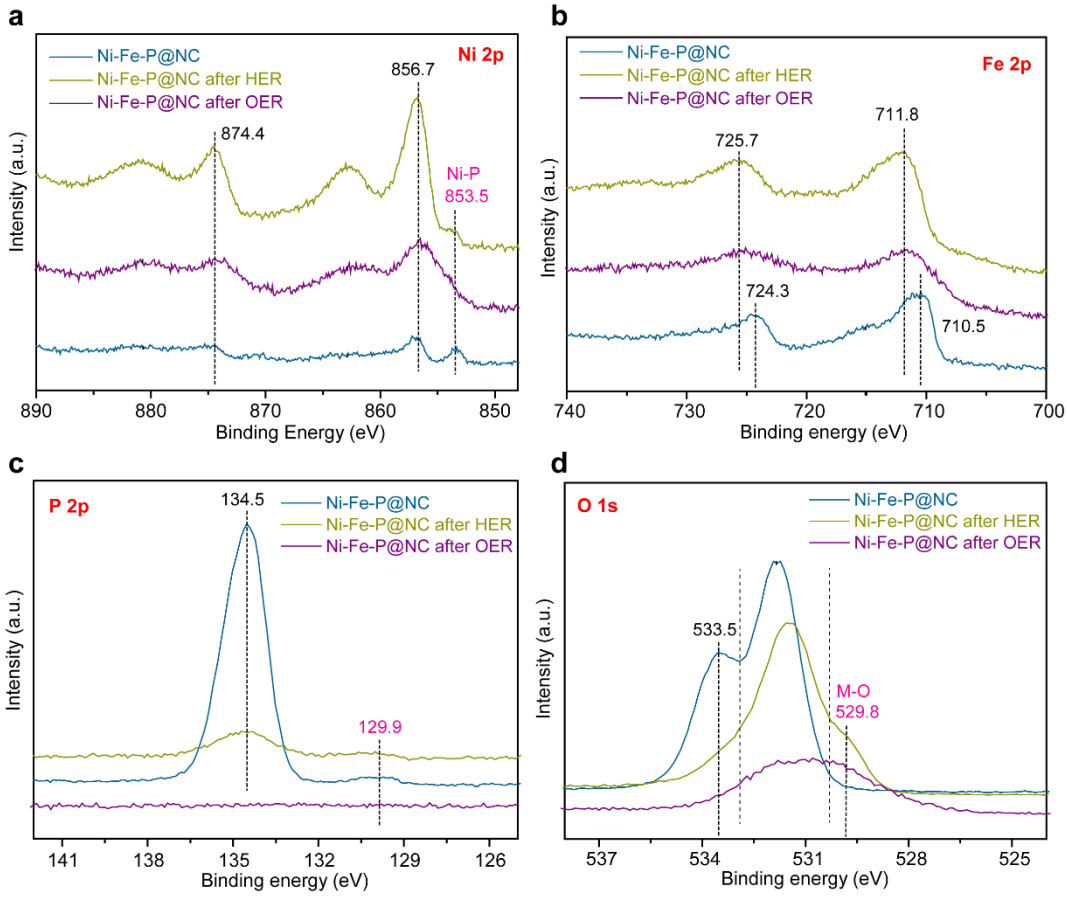

Figure S16. The XPS patterns of as-prepared Ni-Fe-P@NC sample, showing the signals of (a) Ni 2p, (b) Fe 2p, (c) P 2p and (d) O 1s, related to **Figure 2, 3 & 4**.

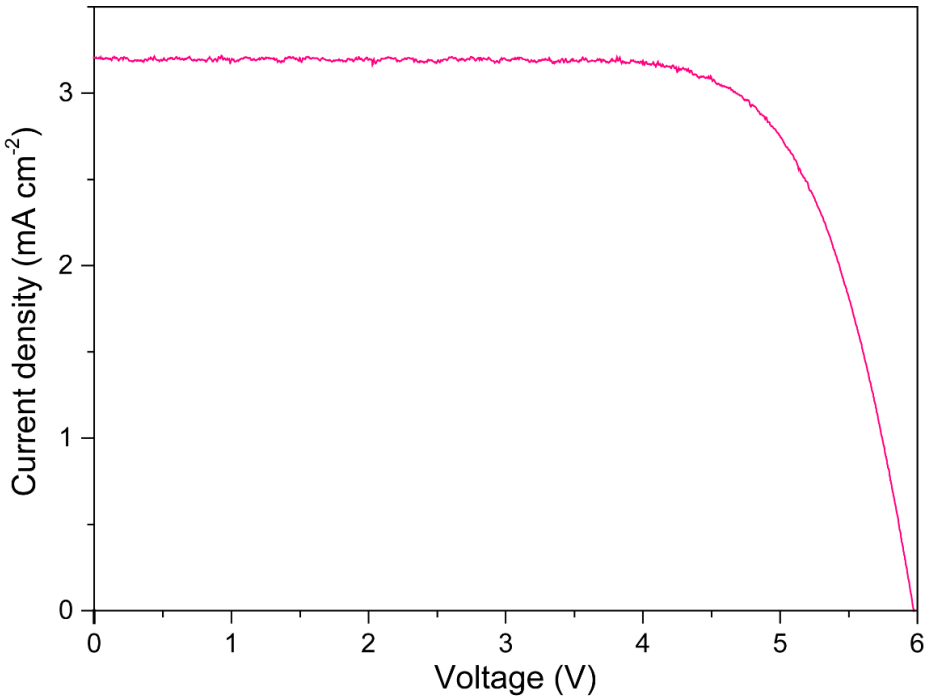

Figure S17. Current-voltage curve of a commercial silicon solar cell under simulated sunlight (1-sun illumination), related to **Figure 5**.

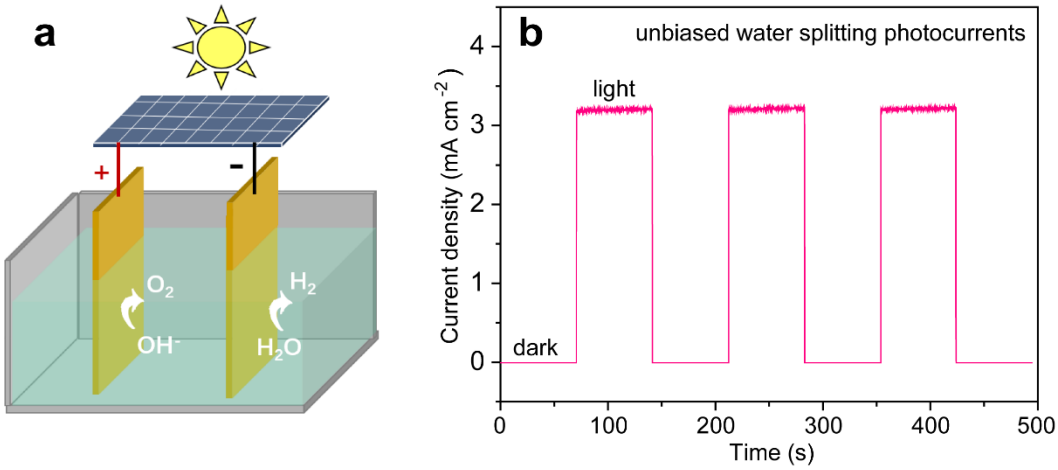

Figure S18. (a) Schematic diagram cell for photo water splitting. (b) Current density-time curve of the PV-EC device (1.0 M KOH) without external bias under chopped simulated AM 1.5 G 100 mW cm^{-2} illumination, related to **Figure 5**.

Table S1. ICP-MS result of Mo in Ni-Fe-P@NC, related to **Figure 1**.

Analyte	Mean Corrected Intensity	Calib. Conc. Units	Std. Dev.	Sample Conc. Units	Std. Dev.	RSD
Mo 202.031	2493.3	0.044 mg/L	0.0004	0.044 mg/L	0.0004	0.81%

As the concentration of the solution was 5 mg/L, the mass concentration of Mo in the solution or the sample was: w (Mo)= 0.044/5 = 0.88% which demonstrates the total conversion from $NiMoO_4$ to $KNiFe(CN)_6$.

Table S2. Values of elements circuit (**Fig. S8**) resulted from fitting the EIS data at -0.2 V *vs* RHE, related to **Figure 3**.

R_s (Ω)	Q_c ($F \cdot s^{(a-1)}$)	a_c	R_c	Q_{ct} ($F \cdot s^{(a-1)}$)	n_{ct}	R_{ct} (Ω)
0.7201	0.4107	0.5521	0.1093	0.2093	0.8502	0.6887

Table S3. Comparison of HER activity for Ni-Fe-P@NC/NF and well-known Ni/Fe-based catalysts in 1.0 M KOH, related to **Figure 3**.

Catalysts	Substrate	η @ -10 mA cm^{-2} (mV)	Tafel slope (mV dec^{-1})	References
Ni-Fe-P@NC	**Ni foam**	**65**	**81.0**	**This work**
Ni_2P@$FePO_x$	Ni foam	75	67	*Chem. Sci.,* **2018**, 9, 1375
NiFe NTAs	Ni foam	181	147.0	*ACS Appl. Energy Mater.* **2018**, 1, 3, 1210-1217
Ni/NiFe (oxy)hydroxide	Ni foam	210	71	*ACS Appl. Mater. Interfaces* **2018**, 10, 8585−8593
$FePO_4$ NW	Ni foam	42.7	104.5	*Adv. Mater.* **2017**, 29, 1704574
Mesoporous FeS_2[b]	Ni foam	96	78	*J. Am. Chem. Soc.* **2017**, 139, 13604
NiS_2/CoS_2-O NW	CFP	174	45	*Adv. Mater.* **2017**, 29, 1704681
MoS_2/ $Fe_5Ni_4S_8$	FeNi foam	120	45.1	*Adv. Mater.* **2018**, 30, 1803151
2D NiS_2	Ni foam	122	86	*Nano Energy* **2017**, 41, 148
V-doped NiS_2	Glass carbon	110	90	*ACS Nano* **2017**, 11, 11574
NiFe/$NiCo_2O_4$	Ni foam	105	88	*Adv. Funct. Mater.* **2016**, 26, 3515
$Ni_{0.33}Co_{0.67}S_2$ NW	Ti foil	88	118	*Adv. Energy Mater.* **2015**, *5*, 1402031
$Ni_{0.89}Co_{0.11}Se_2$ MNS	Ni foam	85	52	*Adv. Mater.* **2017**, 29, 1606521
Fe-Ni_3S_2/NF	Ni foam	47	95	*ACS Catal.* **2018**, 8, 5431−5441
$Ni_{0.33}Co_{0.67}Se_2$	CFP	106	60	*Adv. Energy Mater.,* **2017**, 7, 1602089
V-doped NiS_2	Glass carbon	110	90	*ACS Nano* **2017**, 11, 11574
NF@Ni/C-600	Ni foam	37	57	*Energy Environ. Sci.,* ***2018****,11, 2363-2371*
$Ni_{0.89}Co_{0.11}Se_2$ MNS	Ni foam	85	52	*Adv. Mater.* **2017**, 29, 1606521
$Ni_{0.33}Co_{0.67}Se_2$	CFP	65	35	*Adv. Energy Mater.,* **2017**, **7**, 1602089
$Ni_{0.8}Co_{0.1}Fe_{0.1}O_xH_y$	Ni foam	85	84.5	*ACS Catal.* **2018**, 8, 5621−5629
Ni_3FeN/r-GO	Ni foam	94	90	*ACS Nano* **2018**, 12, 245−253
Ni@NC-800	Ni foam	70	160	*Adv. Mater.* **2017**, 29, 1605957

Note: NT, Nanotube; NTAs, Nanotube Arrays; NW, Nanowire; MNS, Mesoporous nanosheet; NS, Nanosheet; CFP, Carbon fiber paper. [a]: N. A.=Not available.

Table S4. Comparison of OER activity for Ni-Fe-P@NC/NF and well-known Ni/Fe-based catalysts in 1.0 M KOH, related to **Figure 4**.

Catalysts	Substrate	η @ 10 mA cm^{-2} (mV)	η @ 50 mA cm^{-2} (mV)	η @ 100 mA cm^{-2} (mV)	Tafel slope (mV dec^{-1})	References
Ni-Fe-P@NC	**Ni foam**	**140**	**220**	**260**	**84.6**	**This work**
$Fe(PO_3)_2/Ni_2P$	Ni foam	177	N.A.	N.A.	51.9	*PNAS,* **2017**, 114,5607-5611
$Ni_3Fe_{0.5}V_{0.5}$	CFP	200	N.A.	264	39	*Nat. Comm.,* **2018**, 9, 2885
Fe-Ni@NC-CNTs	Ni foam	202	N.A.	N.A.	45.5	*Angew. Chem.* **2018**, 130, 9059 –9064
MoS_2/ $Fe_5Ni_4S_8$	FeNi foam	204	N.A.	N.A.	28.1	*Adv. Mater.* **2018**, 30, 1803151
$Ni_2P@FePO_x$	Ni foam	205	N.A.	230	32	*Chem. Sci.,* **2018**, 9, 1375
Fe-Ni_3S_2/NF	Ni foam	214	N.A.	249	42	*ACS Catal.* **2018**, 8, 5431−5441
$FePO_4$ NW	Ni foam	218	N.A.	N.A.	42.72	*Adv. Mater.* **2017**, 29, 1704574
Ni:Pi-Fe	Ni foam	220	N.A.	N.A.	37	*Chem. Mater.* **2016**, 28, 5659−5666
Ni(OH)2−CeO2	Carbon paper	220	N.A.	N.A.	81.9	*ACS Nano* **2018**, 12, 6245−6251
NiS_2/CoS_2-O NW	CFP	235	N.A.	N.A.	31	*Adv. Mater.* **2017**, 29, 1704681
$Ni_{0.8}Co_{0.1}Fe_{0.1}O_xH_y$	Ni foam	239	288	N.A.	45.4	*ACS Catal.* **2018**, 8, 5621−5629
NiFe-MOF	Ni foam	240	N.A.	N.A.	34	*Nat. Commun.* **2017**, 8, 15341
Ni_1Fe_2-O	GCE	244	N.A.	N.A.	39	*Adv. Energy Mater.* **2018**, 8, 1701347
NF@Ni/C-600	Ni foam	265	353	N.A.	54	*Energy Environ. Sci.,* **2018**, 11, 2363-2371
Ni_3FeN/r-GO	Ni foam	270	298	N.A.	54	*ACS Nano* **2018**, 12, 245−253

Ni–Co–P HNBs	Ni foam	270	N.A.	N.A.	76	*Energy Environ. Sci.*, **2018,**11, 872-880
$Ni_2P_4O_{12}$	carbon cloth	270	N.A.	N.A.	207	*Adv. Mater.* **2018**, 30, 1705045
Ni@NC-800	Ni foam	280	N.A.	N.A.	45	*Adv. Mater.* **2017**, 29, 1605957
$Ni_{1-x}Fe_xPS_3$@ MXene	GC	282	N.A.	N.A.	36.5	*Adv. Energy Mater.* **2018**, 8, 1801127
V-doped NiS_2	Glass carbon	290	N.A.	N.A.	45	*ACS Nano* **2017**, 11, 11574

CFP: Carbon fiber paper; GCE: glassy carbon electrode

Table S5. Summary of overall-water-splitting performance in 1.0 M KOH of various state-of-the-art Ni/Fe based bifunctional electro-catalysts, related to **Figure 5**.

Bifunctional catalysts	Substrate	$E_{J=10}$ (V)	Durability (h)	References
Ni-Fe-P@NC	**NF**	**1.47**	**100**	**This work**
Ni_2P@$FePO_x$	Ni foam	1.51	100	*Chem. Sci., **2018**, 9, 1375*
$Fe_{0.09}Co_{0.13}$-$NiSe_2$ NS	CFC	1.52	30	*Adv. Mater.* **2018**, 30, 1802121
NiFe LDH/Cu NW	Cu foam	1.54	48	*Energy Environ. Sci.* **2017**, 10, 1820
$FePO_4$ NW	Ni foam	1.54	15	*Adv. Mater.* **2017**, 29, 1704574
Fe-Ni_3S_2/NF	Ni foam	1.54	10	*ACS Catal.* **2018**, 8, 5431−5441
NiFe-MOF	Ni foam	1.55	20	*Nat. Commun.* **2017**, 8, 15341
Holey NiCoP NS	Ni foam	1.56	6	*J. Am. Chem. Soc.* **2018**, 140, 5241
V-doped NiS_2	Ni foam	1.56	20	*ACS Nano* **2017**, 11, 1157
NC-NiCu-NiCuN	Ni foam	1.56	50	*Adv. Funct. Mater.* **2018**, 28, 1803278
NFN-MOF/NF[a]	Ni foam	1.56	30	Adv. Energy Mater. 2018, 8, 1801065
NiFeSP	Ni foam	1.58	20	*ACS Nano* **2017**, 11, 10303
IFONFs-45	Fe foil	1.58	8.3	*Nat. Commun.* **2018**, 9, 1809
$Ni_{0.8}Co_{0.1}Fe_{0.1}O_xH_y$	Ni foam	1.58	50	*ACS Catal.* **2018**, 8, 5621−5629

NiCoP films	Scrap copper wires	1.59	24	*Adv. Energy Mater.* **2018**, 1802615
$Ni_{0.75}Fe_{0.125}V_{0.125}$-LDHs	Ni foam	1.591	15	*Small* **2018**, 14, 1703257
Ni_3FeN/r-GO	Ni foam	1.60	100	ACS Nano 2018, 12, 245−253
Se-$(NiCo)S_x/(OH)_x$ NS	Ni foam	1.6	66	*Adv. Mater.* **2018**, 30, 1705538
Fe-CoP	Ti foil	1.6	40	*Adv. Mater.* **2017**, 29, 1602441
Ni@NC-800	Ni foam	1.6	50	*Adv. Mater.* **2017**, 29, 1605957
Ni-Co-P HNB	Ni foam	1.62	20	*Energy Environ. Sci.,* **2018**,11, 872
Ni_3Se_2/Co_9S_8	Exfoliated graphene foil	1.62	10	Nano Lett. **2017**, 17, 4202
Ni-P	CFP	1.63	100	*Adv. Funct. Mater.* **2016**, 26, 4067
$NiCo_2S_4$ NW	Ni foam	1.63	50	*Adv. Funct. Mater.* **2016**, 26, 4661
Ni_2P NP	Ni foam	1.63	10	*Energy Environ. Sci.* **2015**, 8, 2347
Ni_2Fe_1-O	Ni foam	1.64	10	*Adv. Energy Mater.* **2018**, 8, 1701347
$Ni_{1-x}Fe_xPS_3$@ MXene	Ni foam	1.65	50	*Adv. Energy Mater.* **2018**, 8, 1801127
FeS NS	Iron foam	1.65	50	*Chem* **2018**, 4, 1139
Hierarchical $NiCo_2O_4$	Ni foam	1.65	15	*Angew. Chem. Int. Ed*. **2016**, 55, 6290
Ni-$P(Ni_{11}(HPO_3)_8(OH)_6$	Ni foam	1.65	100	*Energy Environ. Sci.,* **2018**, 11, 1287
$Co_{0.85}Se$/NiFe-LDH	Exfoliated graphene foil	1.67	10	*Energy Environ. Sci.* **2016**, 9, 478
NiFe/$NiCo_2O_4$	Ni foam	1.67	10	*Adv. Funct. Mater.* **2016**, 26, 3515
Ni_5P_4	Ni foil	~1.69	N. A.	*Angew. Chem. Int. Ed.* **2015**, 54, 12361
NiSe	Ni foam	1.69	N.A.	*Adv. Energy Mater.* **2018**, 8, 1702704
NiFe LDH	Ni foam	1.70	10	*Science* **2014**, 345, 1593
$FeSe_2$	Ni foam	1.72	24	*Angew. Chem. Int. Ed.* **2017**, 56, 10506
NiS_2/CoS_2–O	CFP	~1.77	21	*Adv. Mater.* **2017**, 29, 1704681

[a]NFN: NH_2-MIL-88B(Fe_2Ni) MOF

Transparent Methods

Chemicals and synthesis: $NaMoO_4 \cdot 2H_2O$, $Ni(NO_3)_2 \cdot 6H_2O$, NaH_2PO_2, $K_3[Fe(CN)_6]$, $FeSO_4 \cdot 7H_2O$, glycerol, NH_4F, Pt/C, RuO_2 and Nafion 117 solution were purchased from Sigma Aldrich. KOH pellets were purchased from Merck KGaA. MilliQ water with a resistivity ≥ 18 MΩ was used to prepare all aqueous solutions. All the reagents were used without further purification.

Synthesis of $NiMoO_4$ and $NiMoO_4$@PBA-XX on nickel foam

$NiMoO_4$ nanowires were synthesized by a modified hydrothermal method. Firstly, 0.242 g of $NaMoO_4 \cdot 2H_2O$ (1.0 mmol) and 0.291 g of $Ni(NO_3)_2 \cdot 6H_2O$ (1.0 mmol) were mixed together with 33 ml of MilliQ water and stirred for 20 min to obtain a precursor solution. Meanwhile, Ni foam cut into 1.0*3.0 cm^2 was sonicated in 3.0 M HCl for 10 min and then put in the Teflon lined autoclave with the above-prepared solution. Then the autoclave was further placed in an oven at 150°C for 4 h. After the reaction, the green powder was grown on Ni foam (denote as $NiMoO_4$/NF), rinsed for 3 times with distilled water and ethanol and then oven-dried at 80°C.
The prepared $NiMoO_4$/NF was weighed before transferred into a 25 mL-via with 16 mL 8.0 mg/mL of freshly prepared $K_3[Fe(CN)_6]$ solutions. The via contained $NiMoO_4$/NF was put in the oven at 90°C for the different duration (*i.e.* 10, 30, 60 and 120 min) and obtained $NiMoO_4$@PBA-10 min/NF, $NiMoO_4$@PBA-30 min/NF, $NiMoO_4$@PBA-1h/NF and $NiMoO_4$@PBA-2h/NF.

Synthesis of Ni-Fe-P@NC nanotubes on nickel foam

In the process of phosphidation step, two quartz boats, with 0.5 g of NaH_2PO_2 in the left boat and a piece of $NiMoO_4$@PBA-2h/NF (1*1.5 cm^2) in the right one, were placed in a stream of nitrogen in the furnace at 350°C for 2 h, where NaH_2PO_2 acted as the phosphorous source (denoted as Ni-Fe-P@NC/NF) and the CN group in PBA served as the C and N sources.

Synthesis of Ni_5P_4 on nickel foam

According to the method reported by Ge and co-workers(Ge et al, 2018), $Ni(NO_3)_2 \cdot 6H_2O$ (1 mmol, 0.291 g), urea (5 mmol, 0.3 g) and NH_4F (2 mmol, 0.074 g) were dissolved in water (20 mL) to obtain the precursor solution. Then a piece of clean nickel foam (1.0*3.0 cm^2) was palced in a Teflon-lined stainless steel autoclave which was immensed in the precursor solution, followed by heating them at 90°C for 12 h in an electric oven. After rreation, the obtained $Ni(OH)_2$/NF was cut into 1.0*1.5 cm^2 and phosphidated at 350°C for 2 h.

Synthesis of FeP

Accordint to the literature (Wang et al, 2019), $FeSO_4 \cdot 7H_2O$ (0.24g) and glycerol (2.5 mL) were dissolved in water (60 mL) which were further stirred for 30 minutes. Then the obtained solution was transferred into Teflon-lined stainless steel autoclaves, followed by heating them at 110°C for 12 h in an electric oven. After heating, the autoclave was turned off and cooled down naturally to room temperature. Then the target products (α-FeOOH) were collected by centrifugation, followed by drying at 70°C for several hours.
The obtained α-FeOOH and NaH_2PO_2 were mixed together and placed in a quatz boat which was palced in the middle of the oven. The atomic ratio for Fe to P is 1:10. Subsequently, the sample was heated at 350°C for 120 min at a heating rate of 5 ℃ min^{-1} in a flow N_2 atmosphere, and then naturally cooled to the room temperature. The obtained products were washed and collected by centrifugation. Finally, the powders were dried at 60℃ for 12 h.

Material characterizations. Phase fractions were determined using X-ray diffraction (XRD) and the data of all the materials were collected with Co Kα radiation on a Bruker D8 Advance eco diffractometer with a Lynxeye XE energy discrimination position-sensitive detector.
The morphologies of as-prepared samples were characterized by Scanning electron microscopy (SEM) using an FEI Nova NanoSEM at 5 kV. Conventional transmission electron microscopy (TEM) was carried out using a Tecnai T20 Twin operated at 200 kV with samples made by evaporating a drop of dispersions of the sub-micron wires in butanol onto holey-carbon-coated Cu grids. A Tecnai F20 SuperTwin operating at 200 kV was used to obtain scanning transmission electron microscopy (STEM) images and energy-dispersive spectrum (EDS) maps. STEM and TEM employed the same sample preparation process.
The Raman measurements were performed on a Renishaw Invia Raman microscope fitted with 488 nm Modulaser triple line argon-ion laser and a Coherent Inc 633 nm (red) HeNe laser.

"100%" power delivery would correspond to about 1mW on a 1 μm diameter spot of the sample. Use 5-10% of the power is fairly common to reduce the chance of sample heating damage. X-ray photoelectron spectroscopy (XPS) analysis was performed using either an AXIS Nova or an AXIS Ultra spectrometer (Kratos Analytical Inc., Manchester, UK) with a monochromated Al Kα source using the standard aperture (analysis area: 0.3 mm × 0.7 mm).

Pre-treatments for ICP-MS test. PerkinElmer Optima 8300 was apllied for testing the content of Mo in Ni-Fe-P@NC. Standard solutions with a series of concentrations of 0.1, 1, 5 and 10 ppm were prepared and tested to obtain the standard curve. Then 1 mg of sample was weighed and placed in a beaker where 4 mL of aqua regia was added to dissolve the sample. The obtained solution was heated and concentrated to 500 μL and diluted to suitable concentrations such as 100 ppm or 200 ppm. Then solution was further diluted to 5 ppm for ICP-MS test.

***Electrochemical measurements*.** A three-electrode system was set up with Ni-Fe-P@NC/NF (1.0*1.0 cm^2) clipped by a platinum clip as the working electrode, a graphite rod and Hg/HgO as the counter electrode and the reference electrode, respectively, in 1.0 M KOH. To prepare Pt/C and RuO_2 electrode, 10 mg of Pt/C or RuO_2 powders with 1 mL of ethanol and 50 uL of Nafion 117 solution were placed in 1.5 mL vial and was then sonicated for 5 minutes. 300 μL of the obtained Pt/C or RuO_2 suspension were dropped on a piece of Ni foam with a mass loading size of 1.0*1.0 cm^2 and dried in the fume cupboard. The FeP electrode was fabricated by suspending 12 mg of FeP particles in 1 mL of ethonal with 60 μL of Nafion 117 solution by sonication. Then, 0.5 mL of suspension was dropped on the nickel foam (1.0*1.0 cm^2) and dried in the fume cupboard. The electrochemical catalytic activity of Ni-Fe-P@NC/NF in 1.0 M KOH was evaluated by the polarization curves from linear sweep voltammetry (LSV) with a scan rate of 5 mV s^{-1}. All the potential values presented in this work were *iR*-corrected (aiming to remove the ohmic potential drop; $C_{correction} = E_{measure} - iR$) and referenced to the hydrogen electrode (RHE) unless indicated otherwise. The Frequency range for Electrochemical Impedance Spectroscopy (EIS) is from 100 kHz to 10 mHz on SP 150 (BioLogic). For comparison, the same measurements were performed on NF, $NiMoO_4$/NF and NF-P. To study the solar-to-hydrogen conversion, Ni-Fe-P@NC/NF acted as both the anode and cathode in the two-electrode system which connected to a commercial planar silicon photovoltaic (Voc = 6.0 V) working as the power source (illumination by 100 mW cm^{-2} simulated sunlight (1.5 G) for solar-to-hydrogen generation without external bias (Chen et al, 2010; Cox et al, 2014; Kuang et al, 2016; Luo et al, 2014).

Supplemental References

Chen, Z., Jaramillo, T. F., Deutsch, T. G., Kleiman-Shwarsctein, A., Forman, A. J., Gaillard, N., Garland, R., Takanabe, K., Heske, C., Sunkara, M., McFarland, E. W., Domen, K., Miller, E. L., Turner, J. A. & Dinh, H. N. (2010) Accelerating materials development for photoelectrochemical hydrogen production: Standards for methods, definitions, and reporting protocols. *Journal of Materials Research*, 25(1), 3-16.

Cox, C. R., Lee, J. Z., Nocera, D. G. & Buonassisi, T. (2014) Ten-percent solar-to-fuel conversion with nonprecious materials. *Proceedings of the National Academy of Sciences*, 111(39), 14057-14061.

Ge, Y., Dong, P., Craig, S. R., Ajayan, P. M., Ye, M. & Shen, J. (2018) Transforming Nickel Hydroxide into 3D Prussian Blue Analogue Array to Obtain Ni2P/Fe2P for Efficient Hydrogen Evolution Reaction. *Advanced Energy Materials*, 8(21), 1800484.

Kuang, M., Han, P., Wang, Q., Li, J. & Zheng, G. (2016) CuCo Hybrid Oxides as Bifunctional Electrocatalyst for Efficient Water Splitting. *Advanced Functional Materials*, 26(46), 8555-8561.

Luo, J., Im, J.-H., Mayer, M. T., Schreier, M., Nazeeruddin, M. K., Park, N.-G., Tilley, S. D., Fan, H. J. & Grätzel, M. (2014) Water photolysis at 12.3% efficiency via perovskite photovoltaics and Earth-abundant catalysts. *Science*, 345(6204), 1593-1596.

Wang, F., Fang, B., Yu, X. & Feng, L. (2019) Coupling Ultrafine Pt Nanocrystals over the Fe2P Surface as a Robust Catalyst for Alcohol Fuel Electro-Oxidation. *ACS Applied Materials & Interfaces*, 11(9), 9496-9503.